



HAL
open science

Confinement determines transport of a reaction-diffusion active matter front

Nicolas Lobato-Dauzier, Ananyo Maitra, André Estevez-Torres,
Jean-Christophe Galas

► To cite this version:

Nicolas Lobato-Dauzier, Ananyo Maitra, André Estevez-Torres, Jean-Christophe Galas. Confinement determines transport of a reaction-diffusion active matter front. 2024. hal-04800819

HAL Id: hal-04800819

<https://hal.science/hal-04800819v1>

Preprint submitted on 24 Nov 2024

HAL is a multi-disciplinary open access archive for the deposit and dissemination of scientific research documents, whether they are published or not. The documents may come from teaching and research institutions in France or abroad, or from public or private research centers.

L'archive ouverte pluridisciplinaire **HAL**, est destinée au dépôt et à la diffusion de documents scientifiques de niveau recherche, publiés ou non, émanant des établissements d'enseignement et de recherche français ou étrangers, des laboratoires publics ou privés.

Main Manuscript for

Confinement determines transport of a reaction-diffusion active matter front

Nicolas Lobato-Dauzier^{1*}, Ananyo Maitra^{1,2}, André Estevez-Torres^{1,3*}, Jean-Christophe Galas^{1*}

¹ Sorbonne Université, CNRS, Institut de Biologie Paris-Seine (IBPS), Laboratoire Jean Perrin (LJP), F-75005, Paris

² CY Cergy Paris Université, CNRS, Laboratoire de Physique Théorique et Modélisation, 95032 Cergy-Pontoise, France

³ Université de Lille, CNRS, Laboratoire de spectroscopie pour les interactions, la réactivité et l'environnement (UMR 8516 - LASIRE), F-59655, Villeneuve d'Ascq, France

***Corresponding authors:** Nicolas Lobato-Dauzier, André Estevez-Torres, Jean-Christophe Galas

Email: {nicolas.lobato-dauzier ; andre.estevez-torres ; jean-christophe.galas}@sorbonne-universite.fr

Author Contributions: NL, AM, AET, JCG designed the research. NL performed the experiments and analyzed the data. AM performed the analytical modelling. NL, AM, AET, JCG wrote the paper.

Competing Interest Statement: No competing interests.

Classification: Applied physical sciences (Biophysics and Computational Biology)

Keywords: Active turbulence, microtubule-kinesin, pattern formation, chemomechanics

This PDF file includes:

Main Text

Figures 1 to 4

Abstract

Couplings between biochemical and mechanical processes have a profound impact on embryonic development. However, in-vitro studies capable of quantifying these interactions have remained elusive. Here, we investigate a synthetic system where a DNA reaction-diffusion (RD) front is advected by a turbulent flow generated by active matter (AM) flows in a quasi-one-dimensional geometry. Whereas the dynamics of simple RD fronts solely depend on the reaction and diffusion rates, we show that RD-AM front propagation is also influenced by the confinement geometry. We first experimentally dissected the different components of the reaction-diffusion-advection process by knocking out reaction or advection and observed how RD-AM allows for faster transport over large distances, avoiding dilution. We then show how confinement impacts active matter flow: while changes in instantaneous flow velocities are small; correlation times are dramatically increased with decreasing confinement. As a result, RD-AM front speed increased 3 to 9-fold compared to a RD one. This RD-AM experimental model provides a framework for the rational engineering of complex spatiotemporal processes observed in living systems. It will reinforce our understanding of how macro-scale patterns and structures emerge from microscopic components in non-equilibrium systems.

Significance Statement

Collections of molecules that react and diffuse create spatial patterns that may be used in living systems to provide positional information. Other collections of molecules, often made of filaments and molecular motors, generate mechanical forces that induce active flows in a closed container. These two processes are ubiquitously coupled in living systems. We designed a non-living experiment to study such coupling where the simplest reaction-diffusion pattern, a front, propagates in a solution of active flows. We found that the front propagates faster and blurs when the width of the container increases, which is not observed for classical reaction-diffusion fronts. This mechanism could be used in vivo for accelerating the transport of biochemical information.

Introduction

Do cells and embryos harness confinement to optimize transport of chemical cues? Transport is singularly important during morphogenesis¹ where it can be achieved via diffusion, reaction-diffusion (RD) or advection by active flows². However, the intrinsic complexity of living embryos³ has led biophysicists and biochemists to develop synthetic systems where these transport mechanisms can be coupled in order to investigate general principles. Here we couple reaction-diffusion and active flows and show that confinement plays a major role in how transport occurs.

While transport by diffusion is fast at short length scales, it becomes slow at long distances as it scales with the square root of time. Two mechanisms allow going beyond this limitation. On the one hand, RD fronts allow for long range transport at a constant velocity when an autocatalytic reaction sustains concentration levels^{4,5}. RD fronts have been observed in a range of chemical systems from inorganic chemistry⁶, to synthetic biochemical circuits⁷⁻¹⁰. DNA computing has proven to be a versatile tool to engineer RD patterns¹¹⁻¹³. Adding enzymes^{14,15} has enabled to program tunable RD fronts¹⁶ and a variety of complex structures such as spiral waves¹⁷, go-fetch fronts¹⁸ and french flag patterns¹⁹. On the other hand, active flows provide a transport mechanism that is independent of both reaction and diffusion for a given chemical. In vivo they may arise from a coupling between two types of cytoskeleton proteins: filaments and motors. In vitro systems combining such cytoskeletal proteins form active gels that share many similarities with living tissues²⁰, forming a variety of patterns²¹⁻²⁵ and flows, either chaotic²⁶ or coherent ones²⁷.

The coupling between advection and reaction-diffusion has mainly been studied for inertial flows^{27,28}. In particular, work has focused on inertial turbulence^{28,29} where hydrodynamic energy cascades down the spatial scales. The conclusion is that inertial turbulence aids the propagation of the reaction front. While such speed-up would undoubtedly be useful in multiple microbiological contexts, but, because microbiological materials have very small Reynolds numbers, they are Stokesian and inertial turbulence is impossible. However, molecular active matter produces a turbulent-like spatiotemporally chaotic state called active turbulence, that creates large-scale flow structures driven by the small-scale injection of energy, potentially inducing a very different transport^{30,31}. In principle, there is no reason why the couplings between active turbulence and reaction-diffusion should resemble those observed for inertial turbulence, though a recent numerical study of reaction-diffusion in a particular model of active, spatiotemporally chaotic fluids has suggested that there are certain similarities in the front dynamics³². Bate, *et al*³³ recently studied the coupling between diffusion and active flows, showing how fast transport of an inert small molecule using sustained turbulent active flows can be, but also how a chemical front cannot be sustained without reaction. Senoussi, *et al*³⁴ introduced reaction-diffusion active matter (RD-AM) fronts, but there the achieved active turbulence did not induce significant transport.

Here we investigate RD-AM fronts in conditions where the transport via active turbulence can be tuned from zero to values that are high enough to significantly perturb the front. Whereas in simple RD fronts, speed and sharpness solely depend on the reaction and diffusion rates, in RD-AM fronts they can be tuned by varying the confinement geometry. This property, that arises from active matter being ruled by geometry-sensitive instabilities³⁵⁻³⁷ could be harnessed in vivo to optimize transport of chemical cues.

Results

Experimental System

Our experiment combines a chemical sub-system incorporating reaction and diffusion and a mechanical sub-system that advects the chemical one via flow³⁴. The former is a single-stranded DNA (ssDNA) coupled to a PEN DNA toolbox^{14,15} autocatalytic reaction (Fig. 1A). The latter consists of microtubule filaments that form bundles in the presence of a depleting agent and are in continuous movement in the presence of clusters of kinesin molecular motors²¹ (Fig. 1B).

The autocatalytic reaction leads to the exponential amplification of ssDNA α , with a reaction rate $r([\alpha])$ that can be modeled with Michaelis-Menten kinetics

$$r([\alpha]) = \frac{V[\alpha]}{K_m + [\alpha]}, \quad (1)$$

where $[\alpha]$ is the concentration of α . We extracted the reaction rate close to 0 from a control experiment in a fluorimeter and obtained a reaction rate constant $k = r'(0) = \frac{V}{K_m} = 0.02 \text{ min}^{-1}$ (see Fig. S1). When α is introduced on one side of a long rectangular channel, the chemical sub-system generates a RD front¹⁶.

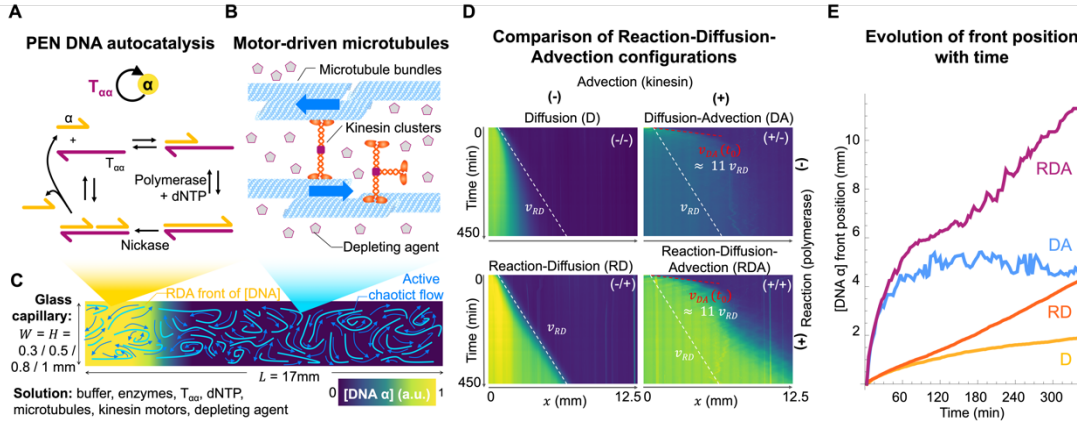


Figure 1 – Experimental setup and its building sub-systems. A: Chemical sub-system. ssDNA is amplified exponentially via a DNA template and enzymes. **B:** Mechanical sub-system. Microtubules bundles slide apart driven by kinesin motors. **C:** Experimental setup. Active chaotic flows interact with a [DNA] front in a closed glass capillary. **D:** Kymographs of DNA concentration of the RD-AM system in different reaction-diffusion-advection regimes. **E:** Evolution of front position over time (threshold chosen at [DNA]=0.2 a.u).

In the mechanical sub-system, kinesins use ATP as a fuel to generate microtubule flows. In this work we use NPE caged-ATP to trigger the activity of motors on demand using UV light³³ (Fig. S2). Both subsystems are mixed and injected into glass capillaries of 17 mm length and varying square sections of 0.3-1 mm widths, plunged in oil to prevent evaporation and observed with a fluorescence microscope (Fig. 1C). A small quantity of DNA α is added on the left side of a channel to trigger the front. Microtubules are fluorescently-labelled and the DNA concentration is monitored thanks to a fluorescent DNA intercalator.

Experimental dissection of the reaction-diffusion-advection model

The whole system can be modeled using a reaction-diffusion-advection (RDA) partial differential equation coupled to a velocity field

$$\frac{\partial[\alpha]}{\partial t} = r([\alpha]) + (\vec{u} \cdot \vec{\nabla})[\alpha] + D_0 \Delta[\alpha], \quad (2)$$

with $[\alpha]$ the DNA concentration, $r([\alpha])$ the reaction rate, \vec{u} the velocity of the fluid, and D_0 the diffusion coefficient. In order to experimentally study the different contributions of each term in the RDA equation, we successively knocked out reaction and/or advection by suppressing DNA polymerase and/or kinesin motors.

When both kinesin and DNA polymerase are absent, α diffuses freely (Figs. 1D top left and S3). Transport slows down quickly and the concentration front is nearly stopped after ~ 2 mm. From this experiment we extracted the diffusion coefficient $D_0 = 1.9 \cdot 10^3 \mu\text{m}^2/\text{min}$, in agreement with previous work¹⁶. Adding polymerase turns on the DNA autocatalytic reaction and generates a reaction-diffusion (RD) front propagating with constant speed $v_{RD} = 12.6 \mu\text{m}/\text{min}$ and width $\delta_{RD} = 0.3$ mm (Figs. 1D bottom left and S4), as previously reported¹⁶. The Fisher-Kolmogorov-Petrovskii-Piskunov¹⁴ (FKPP) model predicts the speed of such RD fronts to be

$$v_{FKPP} = 2\sqrt{kD}, \quad (3)$$

where k is the reaction rate constant and D the diffusion coefficient. The associated width is given by

$$\delta_{FKPP} = \sqrt{\frac{D}{k}}. \quad (4)$$

Using $k = r'(\alpha)$ and $D = D_0$ we find $v_{FKPP} = 12.4 \mu\text{m}/\text{min}$ and $\delta_{FKPP} = 0.3$ mm, in excellent agreement with the experimental values. Eq. (4) means that for a given chemistry (i.e. k fixed), any gain in speed via a change in D_0 involves also an increase in the width of the front. We will see in the following that advection allows for a decoupling of v and δ .

A diffusion-advection (DA) system can be obtained in the presence of kinesin and in the absence of polymerase (Figs. 1D top right and S5). Advection allows for fast long-range transport. At short times, the speed is 11-fold higher than in the RD system. But this induces a dilution, which attenuates the signal making its use in further downstream computation impossible. We observe that the DA front is stopped half-way through the channel. This sharp stoppage looks like a flow barrier that blocks substantial concentrations of DNA to be advected further.

When both polymerase and kinesin are present (Figs. 1D bottom right and S6), the RD front propagates within an active convective medium. This reaction-diffusion-active matter (RD-AM) front resembles the DA front at short times ($t < 30$ min). However, in contrast with DA, the reaction term allows, on the one hand, the DNA concentration to recover behind the front and, on the other hand, to reach a high steady state at long times. The RDA front shares with the RD one a sustained DNA concentration behind the front but a speed that is clearly not constant and a seemingly larger width (Fig. S6).

Effect of confinement on active turbulent flows

Confinement is known to dramatically change active-matter systems^{35–39}, in contrast to reaction-diffusion ones. In particular, channel width has been reported to induce a transition from locally chaotic to coherent flows in microtubule-kinesin active matter²⁷. In Wu *et al*, coherent flows in the XY plane were possible because of the closed loop geometry used. This result is not directly transposable to our 17 mm long straight capillaries.

To study more in depth the impact of confinement in the active advection flows, we followed fiducial fluorescent beads (Figs. 2, S7-8, Movies S2-3) for the mechanical sub-system alone in square channels of different widths W . At first glance, the beads trajectories are very different in the highly confined channel ($W = 0.3$ mm) compared to the wider channel ($W = 1$ mm, Fig. 2A). In the former, the bead trajectories are eddies of a typical length of 0.5 mm. In the latter, trajectories are much more rectilinear, the flow velocity along x not changing sign for up to 4 mm. This result is not trivial as one could expect the boundaries to funnel trajectories in the longitudinal direction or confinement to allow less directional changes. We observe the opposite. However, the average instantaneous speed of beads along the x axis remains relatively constant irrespective of the channel geometry (Fig 2B), with a slight increase of the median velocity u_x . In contrast, the bead velocity correlation time τ_{cor} , which accounts for the changes in direction is strongly affected by channel width (Fig. 2C): it is nearly 10 times larger in the 0.8 mm and 1 mm channels compared to the 0.3 mm and 0.5 mm ones. The 0.8 mm channel has the largest correlation time (10% more than the 1 mm channel). From the beads average velocity $\langle u_x \rangle \approx 50$ $\mu\text{m}/\text{min}$ and correlation times τ_{cor} we can extract a characteristic length $l_v = \langle u_x \rangle \cdot \tau_{cor}$ for the vortexes. $l_v \approx 150$ μm in the 0.3 and 0.5 channels and $l_v \approx 1.5$ mm in the larger 0.8 and 1 mm channels.

Fig. 2D further shows the average orientation of the velocity vector for the two extreme channel widths. Red areas correspond to zones where beads move along the x axis, while blue ones correspond to a motion in the transverse direction. In the 0.3 mm channel such zones are numerous, small and not very sharply defined whereas in the 1 mm channel we easily observe two red zones on each side and a blue zone in the middle.

Considering the channel as a 1D system, bead transport is only achieved in the red zones. Blue zones act as hard to cross barriers that force most beads to switch directions. Although the actual flow field is quite complex, these results suggest that it is mainly constituted of two convective cells with beads switching directions on each side and in the middle (Fig. S8 Movies S2-3).

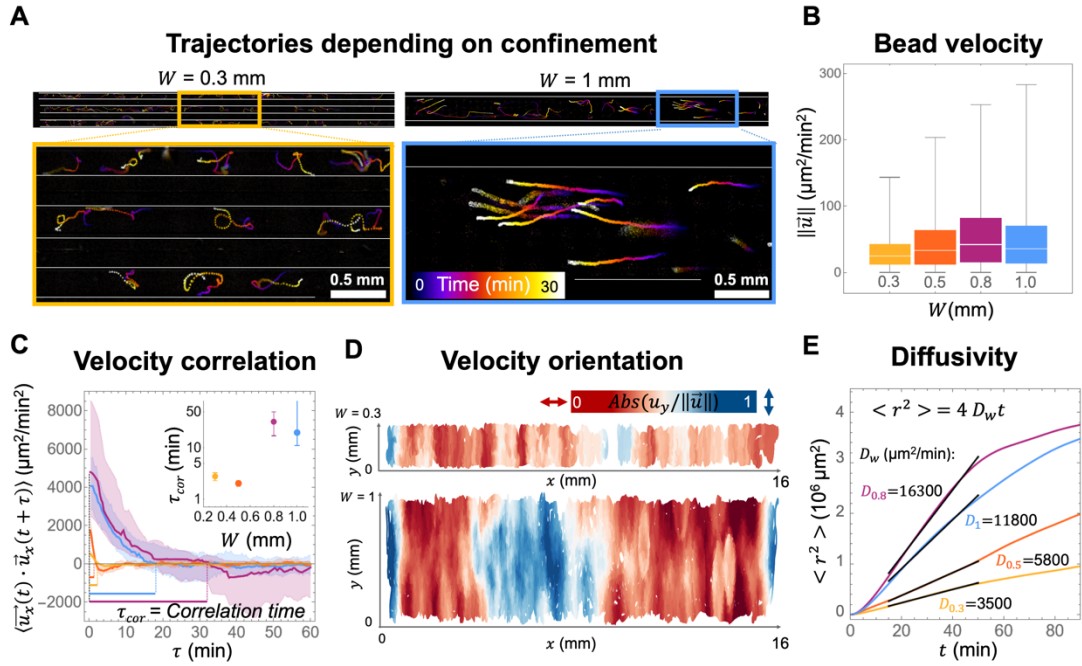


Figure 2 – Characterization of chaotic active flows in closed channels of different widths.
A: Trajectories followed with fiducial beads in square channels of 0.3 mm (left) and 1 mm width (right). Time is color coded from purple to white. **B:** Bead velocity along the x axis for different channel widths. **C:** Bead velocity correlation along the x axis vs. time. Correlation time is the time needed to reach 0 correlation. The inset shows correlation time vs W . **D:** Average bead velocity orientation map for the 0.3 mm (top) and 1 mm wide channel (bottom). Red and blue indicate bead velocity norm respectively parallel and orthogonal to the x. **E:** Beads mean square displacement for varying channel width. The colors in panel B, C, E correspond to the channel width as indicated on B.

The movement of the beads can be further characterized by plotting the evolution of their mean square displacement $\langle r^2 \rangle$ over time (Fig. 2E, S9). Figs. 2E and S10 show a ballistic regime ($r \sim t$) at short times and a diffusive one at intermediate times ($r \sim t^{1/2}$). The transition from ballistic to diffusive happens earlier for the two thinner channels (at $t = 5$ min for $W = 0.3-0.5$ mm and at $t = 15$ min for $W = 0.8-1.0$ mm), in agreement with measurements of the correlation time ($\tau_{cor} \approx 3$ min for the 0.3 and 0.5 and $\tau_{cor} \approx 30$ min for 0.8 and 1 mm channels). The diffusive regime holds until $t = 50$ min in all channels, after which transport is subdiffusive, which we interpret as the beads hitting the extremities of the channel. In agreement with the average velocity and correlation time, D_w increases with W up to 0.8 mm and decreases for the 1 mm channel.

In summary, the results in Fig. 2 show a dramatic change in the structure of the flow as the width increases from 0.5 to 0.8 mm. In order to understand this effect, we conducted an analytical investigation of an active fluid model (See Theoretical supplement). In the absence of motor activity, microtubule filaments in our experiment form a nematic state; traditionally, the scale of the flow structures formed when this aligned structure is destroyed by activity^{35,40–42} is taken to be wavelength of the fastest growing mode of the instability λ_f . This strongly depends on the confinement geometry and, following earlier works^{36,43–46}, we show that in a long channel with a square cross-section of size W , it scales with W as

$$\lambda_f^2 = \frac{2 W^2}{\left(\frac{W}{l_a}\right) - 1} \sim W l_a. \quad (5)$$

Here, l_a is a length scale that depends on both active and elastic properties of the gel and, in general, has a complicated dependence on the composition of the gel such as the motor or

microtubule concentration, ATP concentration, microtubule thickness and length etc. In our experiments, the flow gets smoother for larger W which, if the scale of flow structures is indeed given by wavelength of the fastest growing mode, would correspond to an increase of λ_f as W increases. Since λ_f in (5) has a minimum at $W = 2l_a$, we would then have $W \gg 2l_a$, in the experiments, which leads to the scaling $\lambda_f \sim \sqrt{Wl_a}$. While this qualitatively accounts for the observation of having more disordered flows in thinner channels and more regular ones in wider ones, the scaling obtained experimentally (a ≈ 10 -fold increase in vortex size l_v for a ≈ 3 -fold increase in width) seems to correspond more to a square law than a square root one. This scaling is puzzling and not explained by the linear stability analysis and is not even accounted for by assuming that the flow structures assume the largest possible size before the hydrodynamics is cut off by the walls, in which case it would scale as W . A more sophisticated theoretical treatment of active fluids in a three-dimensional channel beyond the instability of the aligned state or a numerical study is required for understanding the detailed flow structures. This requires significant experimental, numerical and theoretical work, however, and is out of the scope of this article.

Effect of confinement on RD-AM fronts

Now that the flow is well characterized we can investigate the coupling with the RD process. Figure 3 shows the propagation of RD-AM fronts for the two limit cases of low and high transport uncovered in Figure 2 ($W = 0.3$ and 0.8 mm), while Fig. S11 provides data for all channel widths. Corresponding microtubules images are presented in Fig. S12. To show that the difference was solely coming from the active chaotic flows, we first let the experiment run with caged-ATP until $t_0 = 77$ min, when it is uncaged with UV light. Before UV exposure, we observe just simple RD fronts that travel at the same speed $v_0 = 9 \pm 1$ $\mu\text{m}/\text{min}$ in all channels. After UV exposure, the dynamics are slightly changed for 0.3 mm, while they are largely disrupted at 0.8 mm. In the thinner 0.3 mm channel, the front speed v_1 is identical to v_0 while the front width δ increases twofold. Both observations are in line with advection happening at a very local level without triggering long-range transport.

In the 0.8 mm channel, right after uncaging, the RD-AM front looks like a turbulent wave, advection increasing 9-fold the front speed, to $v_1 = 85$ $\mu\text{m}/\text{min}$. During this first phase, that lasts 40-50 min, strong inhomogeneities appear in the transverse region: low fluorescence spots behind the front show backward dilution while bright zones ahead of the front indicate forward transport of DNA (Fig 3D). This corresponds to transport by advection in a single hydrodynamic cell, with concentration levels sustained by the reaction. At $t_1 = 110$ -120 min, the front reaches the middle of the channel and it is severely slowed down back to $v_2 = 9$ $\mu\text{m}/\text{min}$, while front width decreases abruptly. We interpret this second phase as the front reaching the limit of a convection cell: advection becomes negligible and the front behaves as an RD one (Fig 2C). However, while v remains constant during this second phase, δ increases steadily, in contrast with the pure RD case. At $t_2 = 280$ min, a third phase appears with a speed v_3 about two-fold the RD one and a low sharpness. Phases 1-3 are similarly observed in the 1 mm channel (Fig S13), although a fourth phase appears at longer times, with an increase in DNA happening almost simultaneously everywhere. Which we interpret as a kinematic wave⁴⁷ of DNA amplification of very dilute concentrations advected across the whole length of the channel. Note that, while for RD fronts the front shape is stationary and its speed does not depend on the chosen concentration level threshold, for RD-AM fronts it is difficult to define the actual position of the front due to its inhomogeneities and instabilities. Choosing different concentration thresholds leads to very different (but coherent) results (Fig. S14).

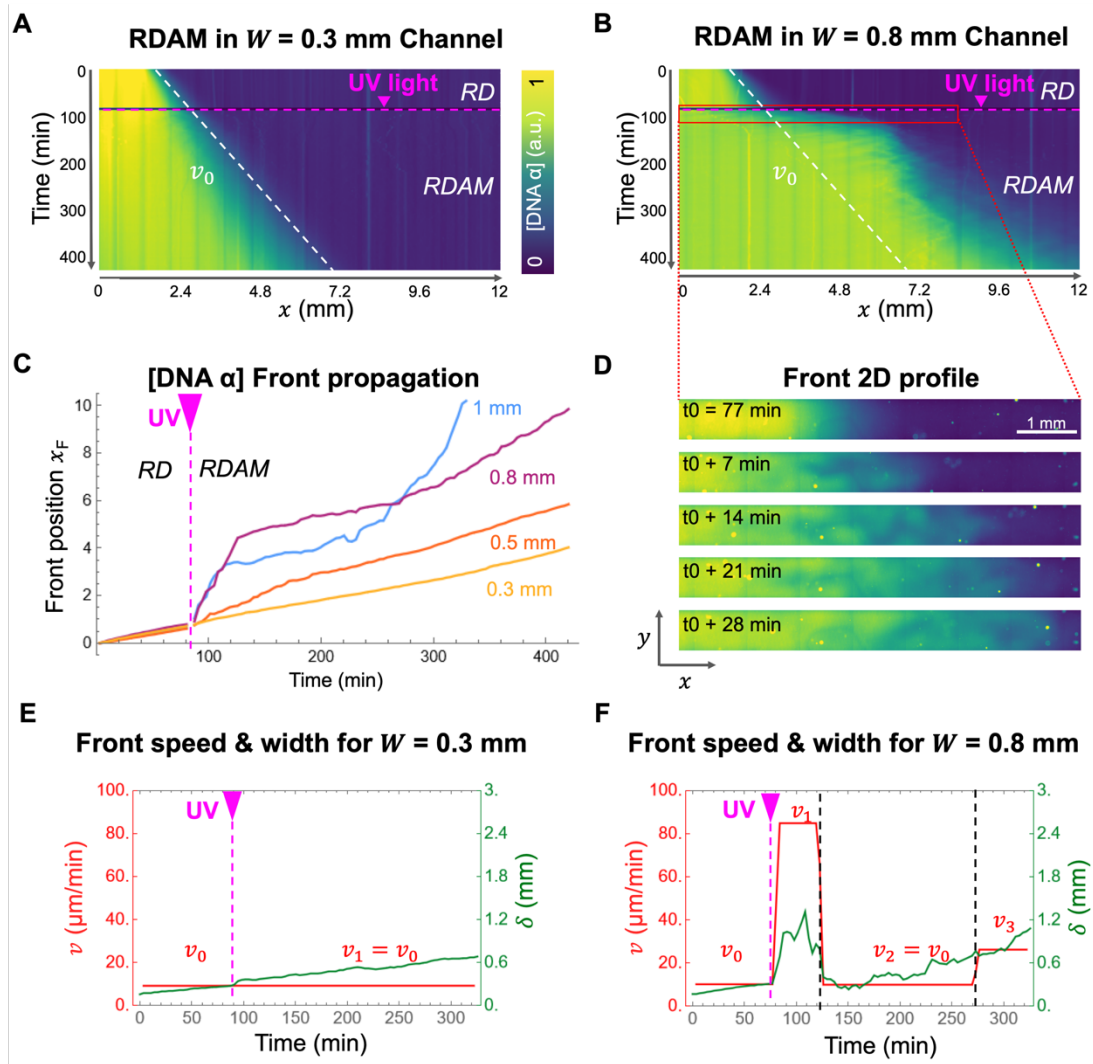


Figure 3- Geometry-dependent Reaction-Diffusion-Advection. **A:** Kymograph of the front propagation in the 0.3 mm width channel. **B:** Kymograph of the front propagation in the 0.8 mm width (See Fig. S11 for the 0.5 mm and 1 mm channels). **C:** Evolution of front position for different channel widths (Threshold 0.5). **D:** Time-lapse fluorescence images showing front 2D profile in the xy plane. **E-F:** Evolution of front speed (left axis, red) and width (right axis, green) for the 0.3 mm (E) and 0.8 mm (F) channel.

Figure 4 sums up the effect of confinement on the propagation speed and sharpness of RD-AM fronts. Figure 4A shows the different speeds obtained in each channel, extracted from a linear piecewise decomposition of Figure 3C (see Figure S14). Before the activity is switched on, the front speed is identical in all channels, irrespective of W , yielding $v_0 = 9 \mu\text{m}/\text{min}$. As stated above, we interpret this speed as a pure RD front, even though it is 30% lower than the v_{RD} measured in Fig. 1D, the difference probably coming from batch to batch variability. Once activity is switched on, several speeds are sequentially measured in the channels. Inspired by the work in inertial⁴⁸ or active³² turbulence, we checked if the FKPP model could describe the dynamics of the RD-AM front when considering the effective dispersion induced by the flow. Figure 4B plots the square of the front speed as a function of the effective dispersion coefficient $D_{eff} = D_0 + D_w$. Using eq. 3 with $D = D_{eff}$ we extrapolated the front speed predicted by the FKPP model from the front speed in the absence of activity v_0 and the diffusion coefficient D_0 , yielding $k = 0.01 \text{ min}^{-1}$ (dashed line in Fig. 4B). In the 0.8 and 1 mm channels, the front speeds v_1 are 8 to 9-fold higher than the FKPP prediction. Indeed, these speeds correspond to transport within a single hydrodynamic cell, which is highly correlated and cannot be modelled as diffusive. The speed v_2 , associated to crossing from one cell to another, is very similar to

the reaction-diffusion speed v_0 and therefore also does not fall on the FKPP extrapolation. Interestingly v_3 , which corresponds to transport in the second hydrodynamical cell and is affected by both ballistic transport within a cell and reaction diffusion to cross from one cell to another, agrees well with the FKPP extrapolation for the 0.8 and 1 mm channels. This is in line with the way D_w was measured with beads in all parts of the channel. In the 0.5 mm channel, hydrodynamic cells are less well defined and v_2 is 40% higher than v_0 , and in fair agreement with the FKPP extrapolation. Finally, in the 0.3 mm case there is no change of the front speed in the presence of active turbulence ($v_1 = v_0$) and therefore no agreement with the FKPP extrapolation. Interestingly, in this case the active flow increases the width of the front without modifying its speed, suggesting a threshold for the flow to accelerate the front speed. Figure 4C shows the trade-off in front speed and sharpness when varying the channel width. The 0.8 mm channel has the best transport performance as the front propagates three times faster than in the regular RD case while the sharpness is only decreased by $\sim 50\%$. When compared to the 0.3 mm channel the speed up is also a factor three and the sharpness loss is only of $\sim 20\%$. To conclude, the transport of RD-AM fronts is complex and associated to an increase of both speed and width when the activity increases as confinement is reduced. The piecewise front speed observed indicates that the process is not captured by a simple FKPP theory. However, we have shown that there exists a regime of transport where the FKPP model is in fair agreement with the measured front speeds (v_2 for 0.5 and v_3 for 0.8-1 mm).

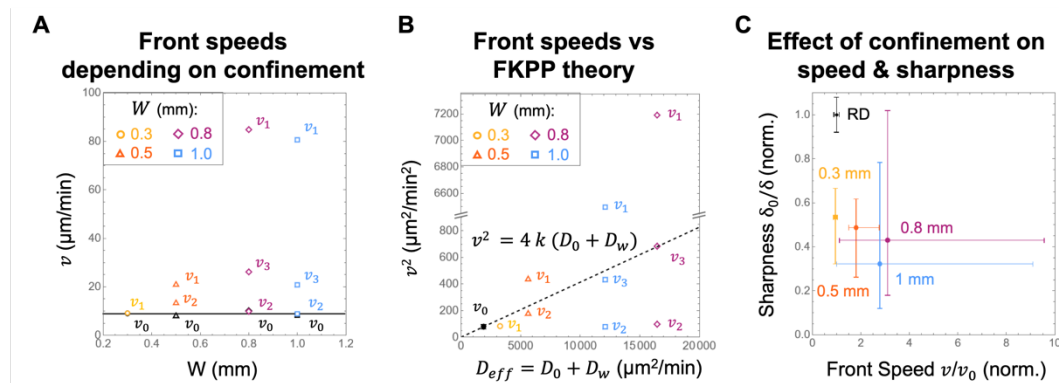


Figure 4 – Geometry-dependent front propagation. **A:** Front speeds vs. channel width. For each width, several front speeds are measured sequentially as in Figure 3F. v_0 is the speed before ATP was uncaged while v_{1-3} correspond to the constant speeds measured at different transport phases. The solid line corresponds to the average of all v_0 . **B:** Square of the front speeds vs. effective diffusion coefficient. The dashed line is a FKPP extrapolation from the RD value yielding $k = 0.01 \text{ min}^{-1}$. **C:** [DNA] front sharpness vs speed for varying channel widths. The dots and the bars correspond respectively to the mean and the extrema values.

Discussion and conclusion

Within cells and embryos, biochemical cues are transported through mechanisms that may combine reaction, diffusion and advection. At this scale, if advection is turbulent it will be generated by active flows and not by inertial ones. While the effect of advection by inertial turbulence on reaction-diffusion dynamics is well understood, little is known about the effect of activity-induced flows on it. We have shown that reaction-diffusion dynamics advected by active flows are strongly geometry-dependent and more complex than RD dynamics advected by turbulent flows. This is due to the nature of active fluid flows which, depending on the confining scale can go from being spatiotemporally chaotic to spatially structured.

We characterized thoroughly chaotic active flows in closed channels of different widths and observed very different and complex flow fields. As channel width increases, the speed of RD-AM fronts increases 3 times on average and up to 9-fold in respect to simple RD fronts while only decreasing sharpness by $\sim 50\%$. With a purely RD mechanism, such an increase in speed

would require elevating the diffusion coefficient or the reaction rate 10-100-fold. Increasing molecular diffusion while maintaining chemical activity is almost impossible while reducing diffusion is possible but hard¹⁶. Increasing k in vivo is possible by mutation. The RDA mechanism that we have elucidated is a simple alternative to accelerate transport without chemically modifying the species at play. In particular, this mechanism could be particularly significant during development where the size increases dramatically and thus, potentially, active flows and their influence in RDA dynamics.

The influence of geometry on active flows has been highlighted previously^{27,35–37,39,45,46,49–54}. Within circular channels, or race-tracks, microtubule-kinesin active matter is known to transition from turbulent to coherent flow when the cross section of the channel is sufficiently symmetric, with the velocity of the coherent flow increasing as the height of the channel increases²⁷. Within rectangular cuboid channels, the activity level and the velocity correlation length have been shown to increase with channel height³⁸. However, in contrast with those experiments happening in pseudo-2D and 3D channels, our pseudo-1D experiments showed both non-null flow velocities and long-time advection transport with coherent eddies or "rivers" sustained for tens of minutes.

The coupling between active matter flows with diffusion or reaction-diffusion has very recently been investigated. With diffusion only, when convective transport dominates mixing is fast but dilution precludes long-range transport³³. When both reaction and diffusion were present, experiments were limited to conditions where convective transport remained limited, similar to our observations in 0.3 mm channels³⁴. Our results are both coherent and extend this previous work.

The crucial role of confinement is best appreciated in the context of the hierarchical architecture observed in adult organisms. For instance, vessel diameters in our vascular system span from cm to μm while in the respiratory system they are in the cm-0.1 mm range. Morphogenesis is responsible for this architecture, which raises a number of questions. Firstly, how does this multi-scale morphogenesis interact with reaction-diffusion processes? Could active transport dramatically transform the landscape of chemical cues and by doing so sharpen the formed shapes? Secondly, as a wide range of signal transport velocities can be achieved solely through confinement, can we ultimately consider it as a biochemical reaction network simplifier? Our results demonstrate that a 3-fold change in the confinement of RD-AM processes, ubiquitous in vivo, have a strong impact on the transport of a chemical cue. They reinforce our understanding of how macro-scale patterns and structures emerge from microscopic components in non-equilibrium systems and may help us engineer living materials with unprecedented properties.

Materials and Methods

Kinesin and Microtubule preparation. We used K401, a truncated kinesin-1 from *Drosophila melanogaster*⁵⁵, which bears a biotin function allowing it to form clusters in the presence of streptavidin²¹. Kinesins were expressed in *E. coli* and purified as previously described²³. Tubulin and TRITC-labeled tubulin (Cytoskeleton) were dissolved at 10 mg/mL in 1× PEM buffer (80 mM Pipes, pH 6.9, 1 mM EGTA, 1 mM MgSO₄) supplemented with 1 mM GTP, flash frozen, and stored at $-80\text{ }^{\circ}\text{C}$. Microtubules were polymerized in 1× PEM, 1 mM GTP, 10% (wt/vol) glycerol, 5 mg/mL tubulin (including 2.5% TRITC-labeled tubulin), 0.5 mg/mL GMPCPP (Jena Bioscience), first at $37\text{ }^{\circ}\text{C}$ for 30 min, then at $25\text{ }^{\circ}\text{C}$ for 5h, flash frozen, and stored at $-80\text{ }^{\circ}\text{C}$.

Active mix preparation. The active mix consisted of (see Table S1) 0.6X PEM buffer (pH = 6.9 KOH adjusted), 0.2X PEM buffer (pH = 7.2 NaOH adjusted), 8 mM MgSO₄, 1.5% (wt/vol) Pluronic F-127, 5 $\mu\text{g}/\text{mL}$ creatine kinase, 10 mM creatine phosphate, 2 mM NPE-Caged ATP, 0.5 mg/mL BSA, 1 mM trolox, 20 mM D-glucose, 3 mM DTT, 150 $\mu\text{g}/\text{mL}$ glucose oxidase, 25 $\mu\text{g}/\text{mL}$ catalase, 10 μM dATP, 25 μM dGTP, 500 μM dCTP, 500 μM dTTP, 0.4X SYBR GreenI, 100 nM DNA template T $\alpha\alpha$, 0 or 1 μM DNA α , 0.5 % (vol/vol) BST Large Fragment polymerase (NEB), 1.5 % (vol/vol) Nt. BstNBI nickase (NEB), 75 nM Kinesin motors, 75 nM Streptavidin, 1 mg/mL Microtubules. DNA sequences (Biomers) are presented in Table S2. For the beads

tracking experiments, T α , DNA α , polymerase and nickase were replaced with 1 μ m diameter beads (Etapor Fluorescent Functionalized Microspheres F1-XC 100, Merck). All elements were pipetted in this order, on ice, except for the addition of microtubules step that was performed at room temperature. Solution was homogenized by a 10s vortexing step before adding the enzymes. Final homogenization was carefully done using the pipette to avoid damaging the microtubules.

Experiments in capillaries. Glass capillaries (Vitrocom) of 50 mm length were cut into 17 mm pieces and coated with an acrylamide brush⁵⁶. They were filled at 95% with the active mix without DNA α and the last 5% with DNA α . Capillaries were immersed in a (70 \times 20 \times 5 mm) glass pool filled with mineral oil to prevent evaporation and keep a homogeneous temperature. The glass pool was placed on a transparent Tokai Hit Thermo Plate set at 24 °C. To ensure thermal equilibrium, this was done 30 min before immersing the capillaries. For ATP uncaging, channels were exposed to UV light with a UV LED (15335337AA350, 365nm, Wurth Elektronik), using a current of 300 mA at \approx 5 mm distance for 3 min.

Imaging. Epifluorescence images were taken on a Zeiss Observer 7 automated microscope equipped with a Andor iXon Ultra camera, a 10X objective (or 4X for beads tracking). The stage is motorized and controlled with MicroManager 1.4. Images were recorded automatically every 3-3.5 min (or 20-30s for beads tracking) using an excitation at 470 nm (for the DNA intercalator SYBR Green I or the beads) and 550 nm for microtubules with a CoolLED pE2 combined to a four bands filter.

Image Analysis. Single images were stitched together and raw fluorescence was normalized to account for different channel thicknesses (See Fig. S17). Time-lapse images were analyzed using Fiji/ImageJ and Mathematica. Beads tracking in Fig. 2 was performed using Trackmate plugin⁵⁷. Definitions of the front width and position are given in Fig S14.

Acknowledgments

We thank Anis Senoussi, Maxime Deforet, Chloe Dal Degan, Romain Leroux, Samuel Bell and Raphaël Voituriez for insightful discussions. This work has been funded by the European Research Council (ERC) under the European's Union Horizon 2020 programme (grant No 770940, A.E.-T.) and ANR LiliMat (ANR-22-CE06-0004, J.-C. G.). A.M. was supported by a TALENT fellowship from CY Cergy Paris Université.

References

- (1) Collinet, C.; Lecuit, T. Programmed and Self-Organized Flow of Information during Morphogenesis. *Nature Reviews Molecular Cell Biology* **2021**, *22* (4), 245–265.
- (2) Burkart, T.; Wigbers, M. C.; Würthner, L.; Frey, E. Control of Protein-Based Pattern Formation via Guiding Cues. *Nature Reviews Physics* **2022**, *4* (8), 511–527.
- (3) Liu, Y.; Xue, X.; Sun, S.; Kobayashi, N.; Kim, Y. S.; Fu, J. Morphogenesis beyond in Vivo. *Nature Reviews Physics* **2023**, 1–17.
- (4) Kondo, S.; Miura, T. Reaction-Diffusion Model as a Framework for Understanding Biological Pattern Formation. *science* **2010**, *329* (5999), 1616–1620.
- (5) Murray, J. D.; Murray, J. D. *Mathematical Biology: II: Spatial Models and Biomedical Applications*; Springer, 2003; Vol. 3.
- (6) Hanna, A.; Saul, A.; Showalter, K. Detailed Studies of Propagating Fronts in the Iodate Oxidation of Arsenous Acid. *Journal of the American Chemical Society* **1982**, *104* (14), 3838–3844.
- (7) Semenov, S. N.; Markvoort, A. J.; de Greef, T. F.; Huck, W. T. Threshold Sensing through a Synthetic Enzymatic Reaction–Diffusion Network. *Angewandte Chemie International Edition* **2014**, *53* (31), 8066–8069.
- (8) Tayar, A. M.; Karzbrun, E.; Noireaux, V.; Bar-Ziv, R. H. Propagating Gene Expression Fronts in a One-Dimensional Coupled System of Artificial Cells. *Nature Physics* **2015**, *11* (12), 1037–1041.
- (9) Loose, M.; Fischer-Friedrich, E.; Ries, J.; Kruse, K.; Schwille, P. Spatial Regulators for

- Bacterial Cell Division Self-Organize into Surface Waves in Vitro. *Science* **2008**, *320* (5877), 789–792.
- (10) Dupin, A.; Simmel, F. C. Signalling and Differentiation in Emulsion-Based Multi-Compartmentalized in Vitro Gene Circuits. *Nature chemistry* **2019**, *11* (1), 32–39.
- (11) Chirieleison, S. M.; Allen, P. B.; Simpson, Z. B.; Ellington, A. D.; Chen, X. Pattern Transformation with DNA Circuits. *Nature chemistry* **2013**, *5* (12), 1000–1005.
- (12) Zenk, J.; Scalise, D.; Wang, K.; Dorsey, P.; Fern, J.; Cruz, A.; Schulman, R. Stable DNA-Based Reaction–Diffusion Patterns. *RSC advances* **2017**, *7* (29), 18032–18040.
- (13) Abe, K.; Murata, S.; Kawamata, I. Cascaded Pattern Formation in Hydrogel Medium Using the Polymerisation Approach. *Soft Matter* **2021**, *17* (25), 6160–6167.
- (14) Montagne, K.; Plasson, R.; Sakai, Y.; Fujii, T.; Rondelez, Y. Programming an in Vitro DNA Oscillator Using a Molecular Networking Strategy. *Molecular systems biology* **2011**, *7* (1), 466.
- (15) Baccouche, A.; Montagne, K.; Padirac, A.; Fujii, T.; Rondelez, Y. Dynamic DNA-Toolbox Reaction Circuits: A Walkthrough. *Methods* **2014**, *67* (2), 234–249.
- (16) Zadorin, A. S.; Rondelez, Y.; Galas, J.-C.; Estevez-Torres, A. Synthesis of Programmable Reaction-Diffusion Fronts Using DNA Catalysts. *Physical review letters* **2015**, *114* (6), 068301.
- (17) Padirac, A.; Fujii, T.; Estévez-Torres, A.; Rondelez, Y. Spatial Waves in Synthetic Biochemical Networks. *Journal of the American Chemical Society* **2013**, *135* (39), 14586–14592.
- (18) Gines, G.; Zadorin, A.; Galas, J.-C.; Fujii, T.; Estevez-Torres, A.; Rondelez, Y. Microscopic Agents Programmed by DNA Circuits. *Nature nanotechnology* **2017**, *12* (4), 351–359.
- (19) Zadorin, A. S.; Rondelez, Y.; Gines, G.; Dilhas, V.; Urtel, G.; Zambrano, A.; Galas, J.-C.; Estevez-Torres, A. Synthesis and Materialization of a Reaction–Diffusion French Flag Pattern. *Nature chemistry* **2017**, *9* (10), 990–996.
- (20) Koenderink, G. H.; Dogic, Z.; Nakamura, F.; Bendix, P. M.; MacKintosh, F. C.; Hartwig, J. H.; Stossel, T. P.; Weitz, D. A. An Active Biopolymer Network Controlled by Molecular Motors. *Proceedings of the National Academy of Sciences* **2009**, *106* (36), 15192–15197.
- (21) Nédélec, F.; Surrey, T.; Maggs, A. C.; Leibler, S. Self-Organization of Microtubules and Motors. *Nature* **1997**, *389* (6648), 305–308.
- (22) Ideses, Y.; Erukhimovitch, V.; Brand, R.; Jourdain, D.; Hernandez, J. S.; Gabinet, U.; Safran, S. A.; Kruse, K.; Bernheim-Groswasser, A. Spontaneous Buckling of Contractile Poroelastic Actomyosin Sheets. *Nature communications* **2018**, *9* (1), 2461.
- (23) Senoussi, A.; Kashida, S.; Voituriez, R.; Galas, J.-C.; Maitra, A.; Estevez-Torres, A. Tunable Corrugated Patterns in an Active Nematic Sheet. *Proceedings of the National Academy of Sciences* **2019**, *116* (45), 22464–22470.
- (24) Sarfati, G.; Maitra, A.; Voituriez, R.; Galas, J.-C.; Estevez-Torres, A. Crosslinking and Depletion Determine Spatial Instabilities in Cytoskeletal Active Matter. *Soft Matter* **2022**, *18* (19), 3793–3800.
- (25) Najma, B.; Varghese, M.; Tsidilkovski, L.; Lemma, L.; Baskaran, A.; Duclos, G. Competing Instabilities Reveal How to Rationally Design and Control Active Crosslinked Gels. *Nature communications* **2022**, *13* (1), 6465.
- (26) Sanchez, T.; Chen, D. T.; DeCamp, S. J.; Heymann, M.; Dogic, Z. Spontaneous Motion in Hierarchically Assembled Active Matter. *Nature* **2012**, *491* (7424), 431–434.
- (27) Wu, W.; Wang, L.; Calzavarini, E.; Schmitt, F. G. Reactive Scalars in Incompressible Turbulence with Strongly out of Equilibrium Chemistry. *Journal of Fluid Mechanics* **2022**, *938*, A19.
- (28) Colombi, R.; Schlüter, M.; Kameke, A. von. Three Dimensional Flows beneath a Thin Layer of 2D Turbulence Induced by Faraday Waves. *Experiments in Fluids* **2021**, *62*, 1–13.
- (29) von Kameke, A.; Huhn, F.; Fernández-García, G.; Muñuzuri, A. P.; Pérez-Muñuzuri, V. Propagation of a Chemical Wave Front in a Quasi-Two-Dimensional Superdiffusive Flow. *Physical Review E* **2010**, *81* (6), 066211.
- (30) Alert, R.; Casademunt, J.; Joanny, J.-F. Active Turbulence. *Annual Review of Condensed Matter Physics* **2022**, *13*, 143–170.
- (31) Martínez-Prat, B.; Ignés-Mullol, J.; Casademunt, J.; Sagués, F. Selection Mechanism at the Onset of Active Turbulence. *Nature physics* **2019**, *15* (4), 362–366.
- (32) Chatterjee, R.; Joshi, A. A.; Perlekar, P. Front Structure and Dynamics in Dense Colonies of Motile Bacteria: Role of Active Turbulence. *Physical Review E* **2016**, *94* (2), 022406.
- (33) Bate, T. E.; Varney, M. E.; Taylor, E. H.; Dickie, J. H.; Chueh, C.-C.; Norton, M. M.; Wu, K.-T. Self-Mixing in Microtubule-Kinesin Active Fluid from Nonuniform to Uniform Distribution of Activity. *Nature communications* **2022**, *13* (1), 6573.
- (34) Senoussi, A.; Galas, J.-C.; Estevez-Torres, A. Programmed Mechano-Chemical Coupling in Reaction-Diffusion Active Matter. *Science Advances* **2021**, *7* (51), eabi9865.
- (35) Voituriez, R.; Joanny, J.-F.; Prost, J. Spontaneous Flow Transition in Active Polar Gels.

- Europhysics Letters* **2005**, 70 (3), 404.
- (36) Chandrakar, P.; Varghese, M.; Aghvami, S. A.; Baskaran, A.; Dogic, Z.; Duclos, G. Confinement Controls the Bend Instability of Three-Dimensional Active Liquid Crystals. *Physical review letters* **2020**, 125 (25), 257801.
- (37) Hardouin, J.; Hughes, R.; Doostmohammadi, A.; Laurent, J.; Lopez-Leon, T.; Yeomans, J. M.; Ignés-Mullol, J.; Sagués, F. Reconfigurable Flows and Defect Landscape of Confined Active Nematics. *Communications Physics* **2019**, 2 (1), 121.
- (38) Fan, Y.; Wu, K.-T.; Aghvami, S. A.; Fraden, S.; Breuer, K. S. Effects of Confinement on the Dynamics and Correlation Scales in Kinesin-Microtubule Active Fluids. *Physical Review E* **2021**, 104 (3), 034601.
- (39) Opathalage, A.; Norton, M. M.; Juniper, M. P.; Langeslay, B.; Aghvami, S. A.; Fraden, S.; Dogic, Z. Self-Organized Dynamics and the Transition to Turbulence of Confined Active Nematics. *Proceedings of the National Academy of Sciences* **2019**, 116 (11), 4788–4797.
- (40) Simha, R. A.; Ramaswamy, S. Hydrodynamic Fluctuations and Instabilities in Ordered Suspensions of Self-Propelled Particles. *Physical review letters* **2002**, 89 (5), 058101.
- (41) Chepizhko, O.; Saintillan, D.; Peruani, F. Revisiting the Emergence of Order in Active Matter. *Soft Matter* **2021**, 17 (11), 3113–3120.
- (42) Maitra, A. Two-Dimensional Long-Range Uniaxial Order in Three-Dimensional Active Fluids. *Nature Physics* **2023**, 1–8.
- (43) Lemma, L. M.; Varghese, M.; Ross, T. D.; Thomson, M.; Baskaran, A.; Dogic, Z. Spatio-Temporal Patterning of Extensile Active Stresses in Microtubule-Based Active Fluids. *PNAS nexus* **2023**, 2 (5), pgad130.
- (44) Varghese, M.; Baskaran, A.; Hagan, M. F.; Baskaran, A. Confinement-Induced Self-Pumping in 3D Active Fluids. *Physical review letters* **2020**, 125 (26), 268003.
- (45) Genkin, M. M.; Sokolov, A.; Lavrentovich, O. D.; Aranson, I. S. Topological Defects in a Living Nematic Ensnare Swimming Bacteria. *Physical Review X* **2017**, 7 (1), 011029.
- (46) Maitra, A.; Srivastava, P.; Marchetti, M. C.; Lintuvuori, J. S.; Ramaswamy, S.; Lenz, M. A Nonequilibrium Force Can Stabilize 2D Active Nematics. *Proceedings of the National Academy of Sciences* **2018**, 115 (27), 6934–6939.
- (47) Epstein, I. R.; Pojman, J. A. *An Introduction to Nonlinear Chemical Dynamics: Oscillations, Waves, Patterns, and Chaos*; Oxford university press, 1998.
- (48) von Kameke, A.; Huhn, F.; Muñuzuri, A. P.; Pérez-Muñuzuri, V. Measurement of Large Spiral and Target Waves in Chemical Reaction-Diffusion-Advection Systems: Turbulent Diffusion Enhances Pattern Formation. *Physical review letters* **2013**, 110 (8), 088302.
- (49) Theillard, M.; Saintillan, D. Computational Mean-Field Modeling of Confined Active Fluids. *Journal of Computational Physics* **2019**, 397, 108841.
- (50) Giomi, L. Geometry and Topology of Turbulence in Active Nematics. *Physical Review X* **2015**, 5 (3), 031003.
- (51) Fürthauer, S.; Neef, M.; Grill, S. W.; Kruse, K.; Jülicher, F. The Taylor–Couette Motor: Spontaneous Flows of Active Polar Fluids between Two Coaxial Cylinders. *New Journal of Physics* **2012**, 14 (2), 023001.
- (52) Wioland, H.; Woodhouse, F. G.; Dunkel, J.; Kessler, J. O.; Goldstein, R. E. Confinement Stabilizes a Bacterial Suspension into a Spiral Vortex. *Physical review letters* **2013**, 110 (26), 268102.
- (53) Woodhouse, F. G.; Goldstein, R. E. Spontaneous Circulation of Confined Active Suspensions. *Physical review letters* **2012**, 109 (16), 168105.
- (54) Suzuki, K.; Miyazaki, M.; Takagi, J.; Itabashi, T.; Ishiwata, S. Spatial Confinement of Active Microtubule Networks Induces Large-Scale Rotational Cytoplasmic Flow. *Proceedings of the National Academy of Sciences* **2017**, 114 (11), 2922–2927.
- (55) Subramanian, R.; Gelles, J. Two Distinct Modes of Processive Kinesin Movement in Mixtures of ATP and AMP-PNP. *The Journal of general physiology* **2007**, 130 (5), 445–455.
- (56) Sanchez, T.; Dogic, Z. Engineering Oscillating Microtubule Bundles. In *Methods in enzymology*; Elsevier, 2013; Vol. 524, pp 205–224.
- (57) Ershov, D.; Phan, M.-S.; Pylvänäinen, J. W.; Rigaud, S. U.; Le Blanc, L.; Charles-Orszag, A.; Conway, J. R.; Laine, R. F.; Roy, N. H.; Bonazzi, D. TrackMate 7: Integrating State-of-the-Art Segmentation Algorithms into Tracking Pipelines. *Nature Methods* **2022**, 19 (7), 829–832.

Supporting Materials for:

Confinement determines transport of a reaction-diffusion active matter front

Nicolas Lobato-Dauzier^{1*}, Ananyo Maitra^{1,2}, André Estevez-Torres^{1*}, Jean-Christophe Galas^{1*}

¹ Sorbonne Université, CNRS, Institut de Biologie Paris-Seine (IBPS), Laboratoire Jean Perrin (LJP), F-75005, Paris

² CY Cergy Paris Université, CNRS, Laboratoire de Physique Théorique et Modélisation, 95032 Cergy-Pontoise, France

³ Université de Lille, CNRS, Laboratoire de spectroscopie pour les interactions, la réactivité et l'environnement (UMR 8516 - LASIRE), F-59655, Villeneuve d'Ascq, France

***Corresponding authors:** Nicolas Lobato-Dauzier, André Estevez-Torres, Jean-Christophe Galas
Email: {nicolas.lobato-dauzier ; andre.estevez-torres ; jean-christophe.galas} @sorbonne-universite.fr

1. SUPPLEMENTARY FIGURES	2
<i>Figure S1 - Extraction of reaction rate</i>	<i>2</i>
<i>Figure S2- Photolytic reaction of NPE caged-ATP. In the presence of UV Light.....</i>	<i>2</i>
<i>Figure S3 – Diffusion.....</i>	<i>3</i>
<i>Figure S4 – Reaction-Diffusion.....</i>	<i>4</i>
<i>Figure S5 – Diffusion-Advection.....</i>	<i>5</i>
<i>Figure S6 – Reaction-Diffusion-Advection.....</i>	<i>6</i>
<i>Figure S8 – Characterization and stability of hydrodynamic flow cells in $W = 1$ mm channel.....</i>	<i>7</i>
<i>Figure S9 – Fiducial beads Mean Square Displacement.....</i>	<i>8</i>
<i>Figure S10 – Power law fits on beads Mean Square Displacement.....</i>	<i>9</i>
<i>Figure S11– Geometry-dependent Reaction-Diffusion-Advection.....</i>	<i>10</i>
<i>Figure S12 – Time-lapse of motor-driven microtubules for varying channel widths.....</i>	<i>11</i>
<i>Figure S13 – Piecewise linear fits of front propagation in channels of different widths.....</i>	<i>12</i>
<i>Figure S14 – Front speed and width depending on definition choices.....</i>	<i>13</i>
<i>Figure S15 – Effect of channel geometry on the evolution of front speed and width.....</i>	<i>14</i>
<i>Figure S16 – Fluorescence normalization taking into accounts the varying channel heights.....</i>	<i>15</i>
2. SUPPLEMENTARY TABLES	16
<i>Table S1: Standard Active mix composition.....</i>	<i>16</i>
<i>Table S2: Sequences of oligonucleotides.....</i>	<i>16</i>
3. LEGENDS OF SUPPLEMENTARY MOVIES S1 TO S4	17
<i>Movie S1 - Comparison of different Reaction-Diffusion-Advection configurations.....</i>	<i>17</i>
<i>Movie S2 –Trajectories of fiduciary beads in channels of different widths.....</i>	<i>17</i>
<i>Movie S3 - Trajectories of fiduciary beads in a 0.8 mm channel at two different heights.....</i>	<i>18</i>
<i>Movie S4 - Geometry-dependent Reaction-Diffusion-Advection.....</i>	<i>18</i>
4. THEORETICAL SUPPLEMENT: Linear stability analysis of aligned active fluids in three-dimensional channels	

1. Supplementary Figures

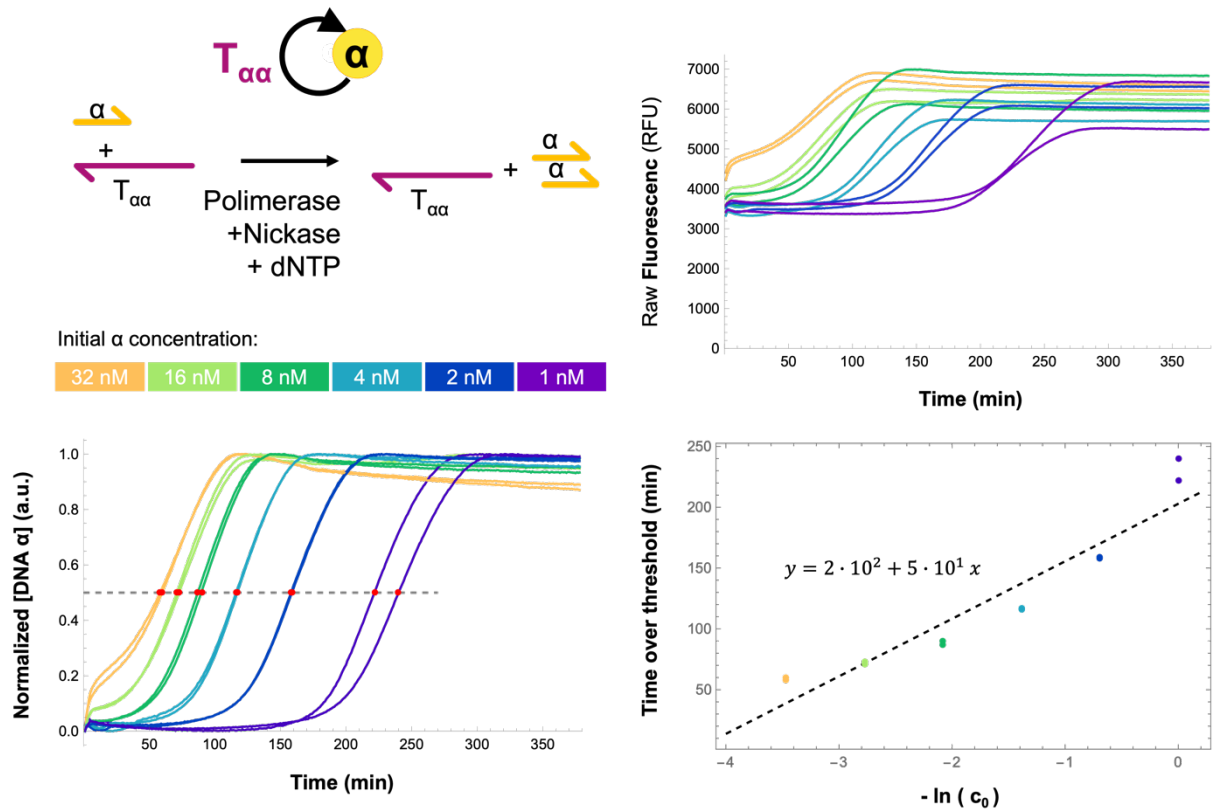


Figure S1 - Extraction of reaction rate. A: PEN DNA Toolbox reaction. B: Raw Fluorescence amplification curves for varying initial α concentration from 1 nM to 32 nM. Acquisition was performed with a CFX96 (Biorad), on 10 μ L of active mix (without microtubules or kinesin). C: Normalized [DNA α] curves. The dashed line corresponds to the thresholding at 50%. D: Amplification times for each initial α concentration. The slope gives $1/k$, the inverse of the reaction rate.

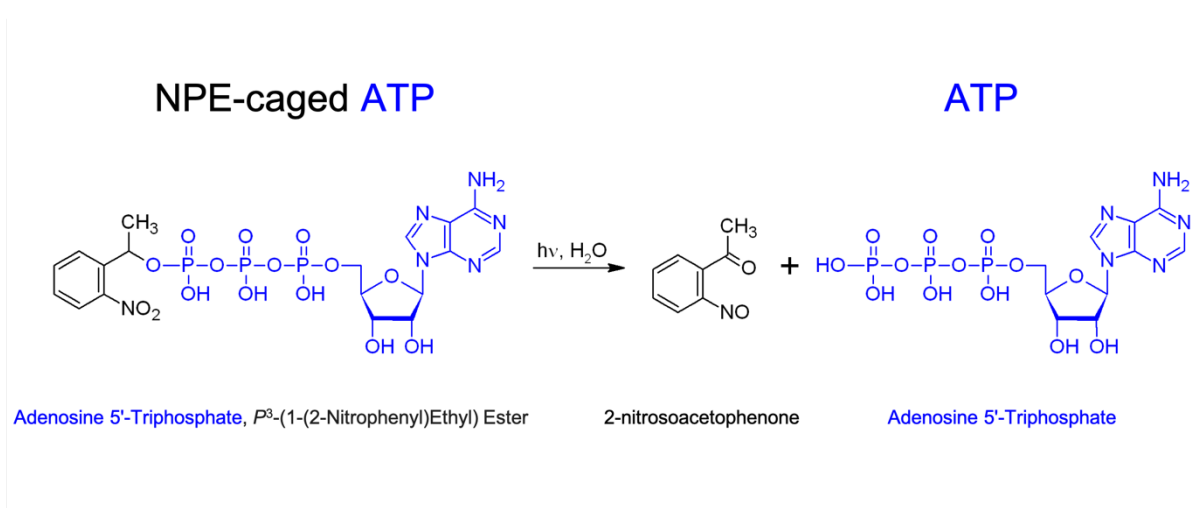


Figure S2- Photolytic reaction of NPE caged-ATP. In the presence of UV Light NPE-caged ATP is dissociated and ATP is released in a usable form. (Adapted from : Wikimedia Commons, Georgwille)

Diffusion

Polymerase (-) / Kinesin (-)

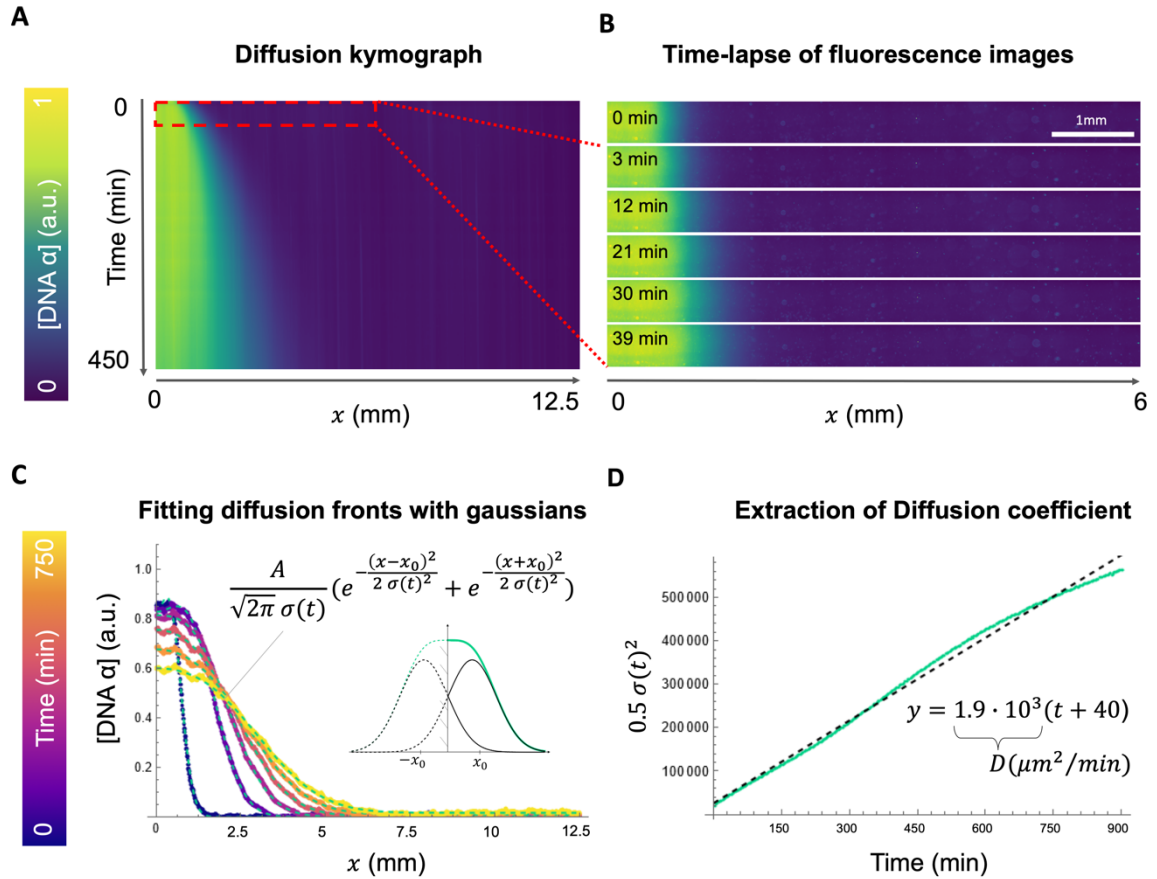


Figure S3 – Diffusion. **A:** Kymograph of DNA concentration diffusion in space over time. **B:** Fluorescence images showing slow transport of DNA by diffusion. **C:** Fitting concentration profiles to obtain the diffusion coefficient. **D:** Extraction of the diffusion coefficient by linear regression.

Reaction-Diffusion

Polymerase (+) / Kinesin (-)

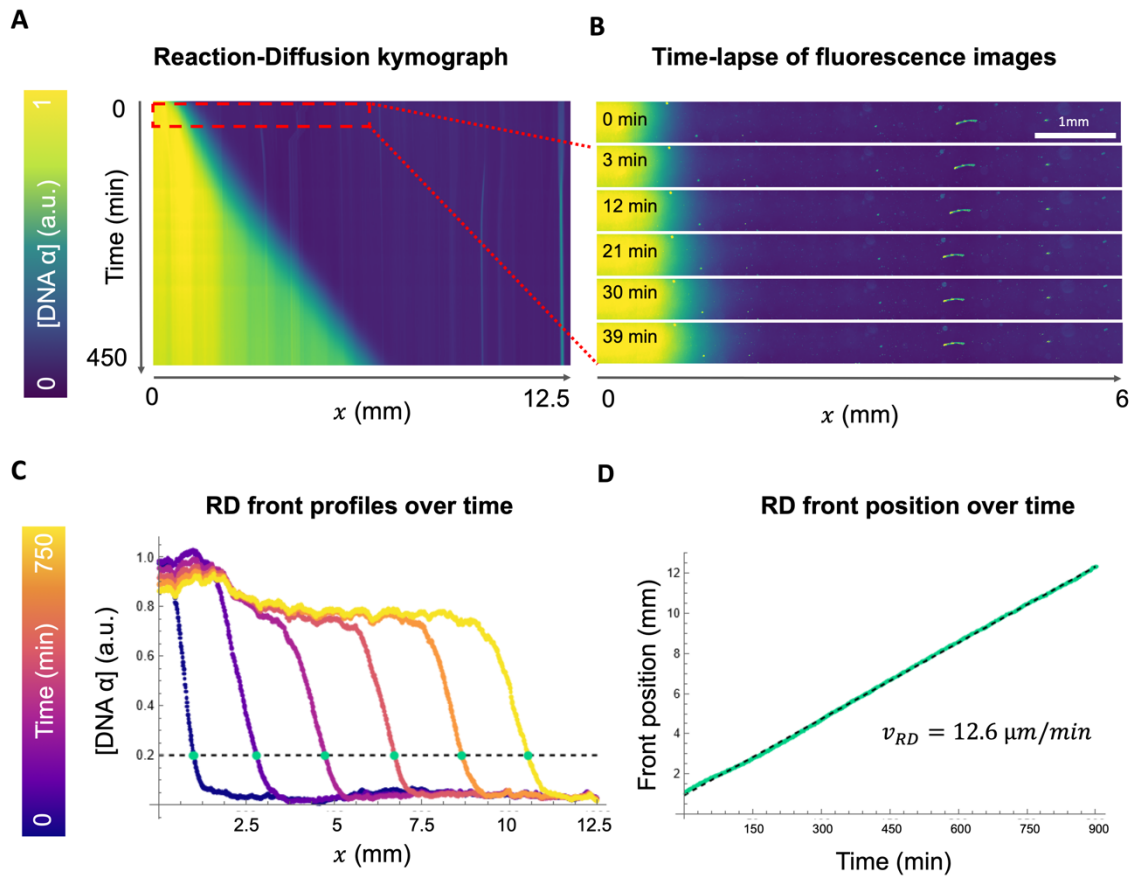


Figure S4 – Reaction-Diffusion. **A:** Kymograph of RD DNA concentration front propagation in space over time. **B:** Fluorescence images showing slow but steady transport of DNA by RD. **C:** Measuring first passage time over 0.2 a.u. threshold to measure front position over time **D:** Extraction of the front propagation speed.

Diffusion-Advection

Polymerase (-) / Kinesin (+)

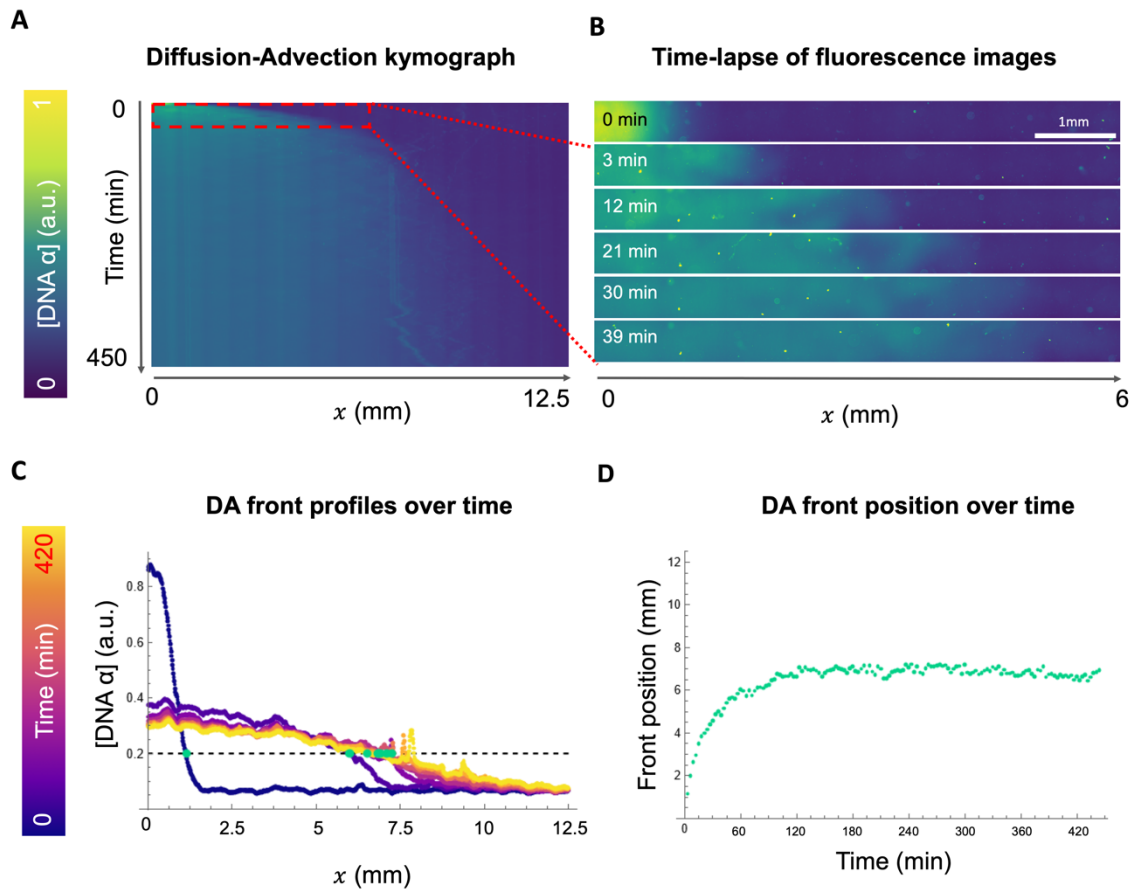


Figure S5 – Diffusion-Advection. **A:** Kymograph of DA DNA concentration front propagation in space over time. **B:** Fluorescence images showing fast short-range transport of DNA by DA. **C:** Measuring first passage time over 0.2 a.u threshold to measure front position over time **D:** Front goes from high velocity on the left to complete stop at the center of the channel.

Reaction-Diffusion-Advection

Polymerase (+) / Kinesin (+)

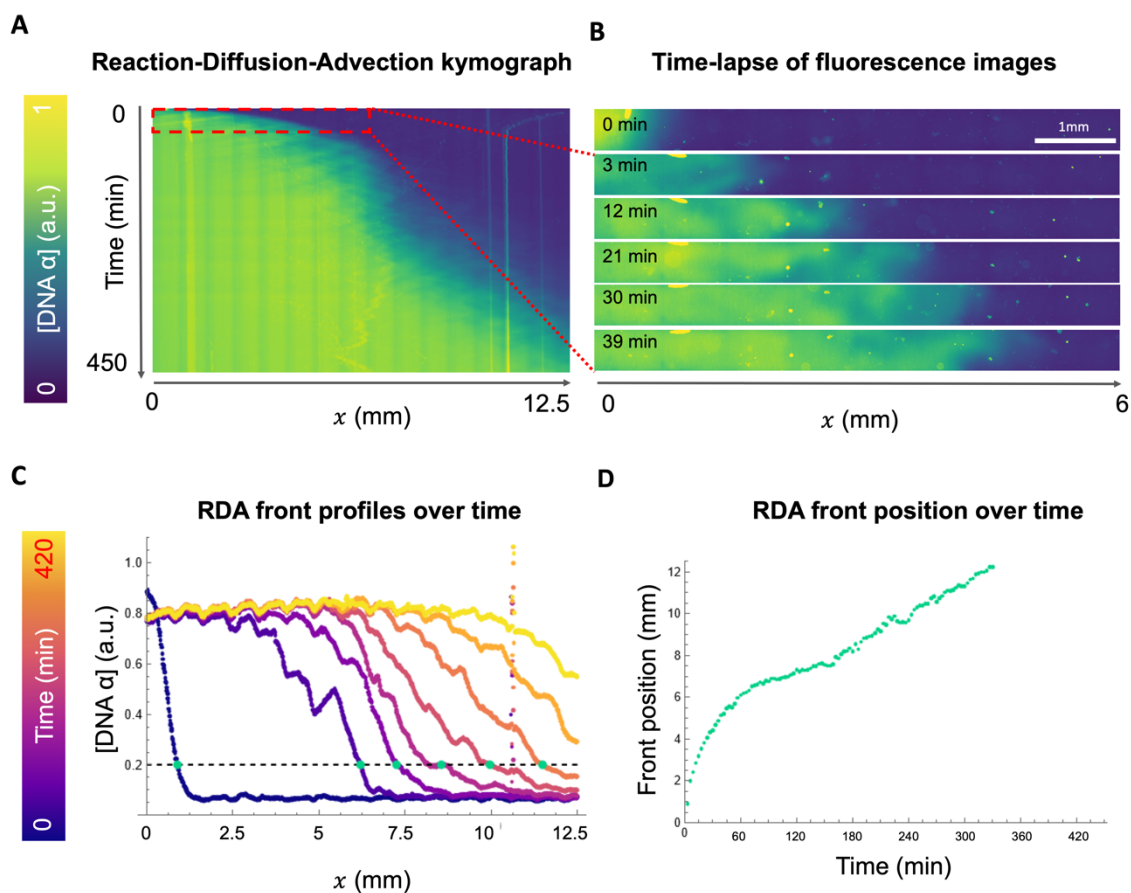


Figure S6 – Reaction-Diffusion-Advection **A:** Kymograph of RDA DNA concentration front propagation in space over time. **B:** Fluorescence images showing fast long-range transport of DNA by RDA. **C:** Measuring first passage time over 0.2 a.u threshold to measure front position over time **D:** Front keeps a high velocity for several hours.

Beads Trajectories in channels of different width

W = 0.3 mm

W = 0.5 mm

W = 0.8 mm

0 30
Time (min)

1 mm

Fig S7 – Beads trajectories over 30 min in square capillaries of width $W = 0.3 / 0.5 / 0.8$ mm. See Movie S2 for full trajectories analyzed in Figure 2

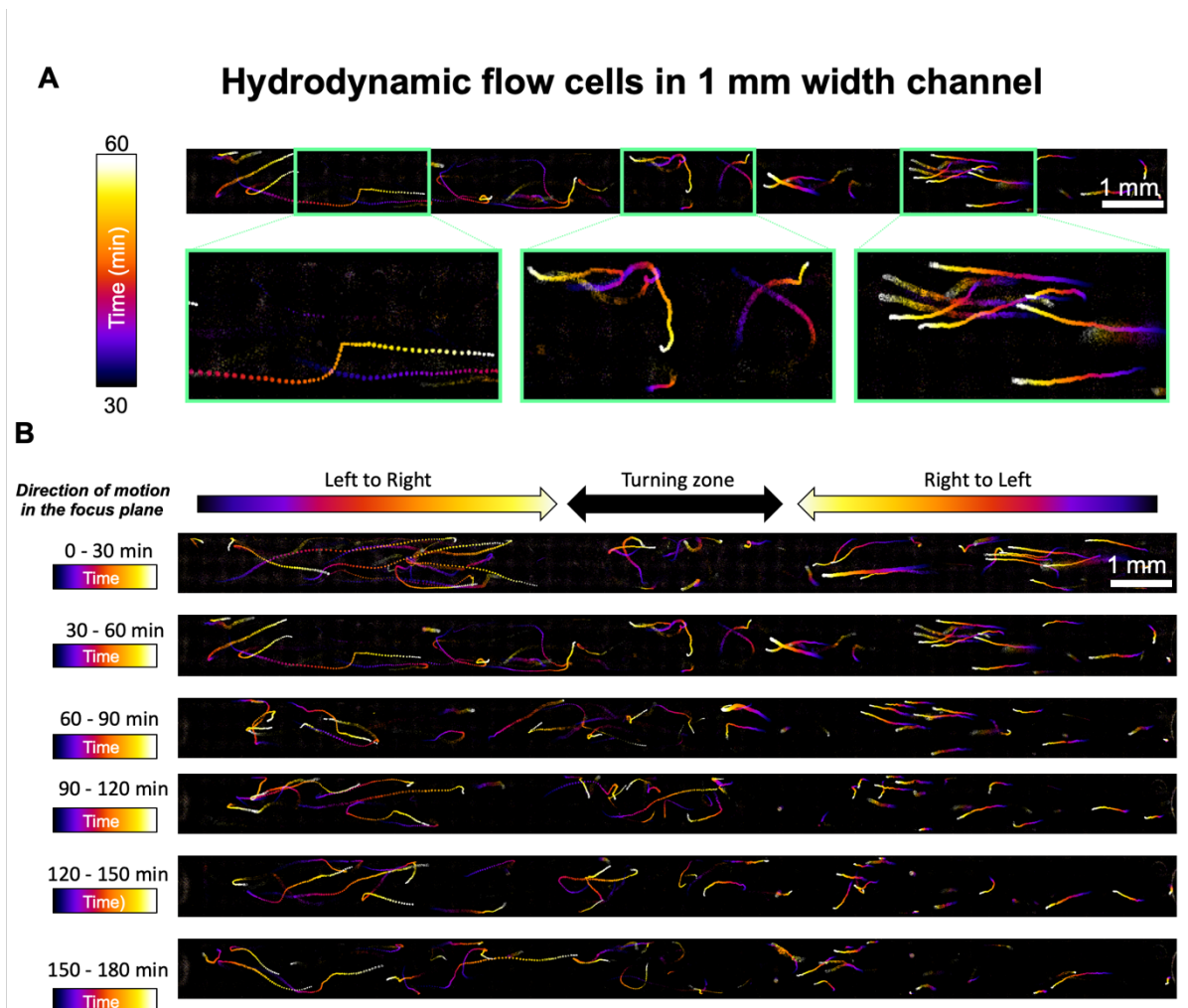


Figure S8 – Characterization and stability of hydrodynamic flow cells in $W = 1$ mm channel. **A:** Beads trajectories between $t = 30$ and $t = 60$ min, color coded by time. We observe two zones (left and right) with motion along the x axis and one zone (center) where beads change direction and move along the y axis. **B:** Stability of the three zones over 3h.

Beads Mean Square Displacement (MSD) over Time

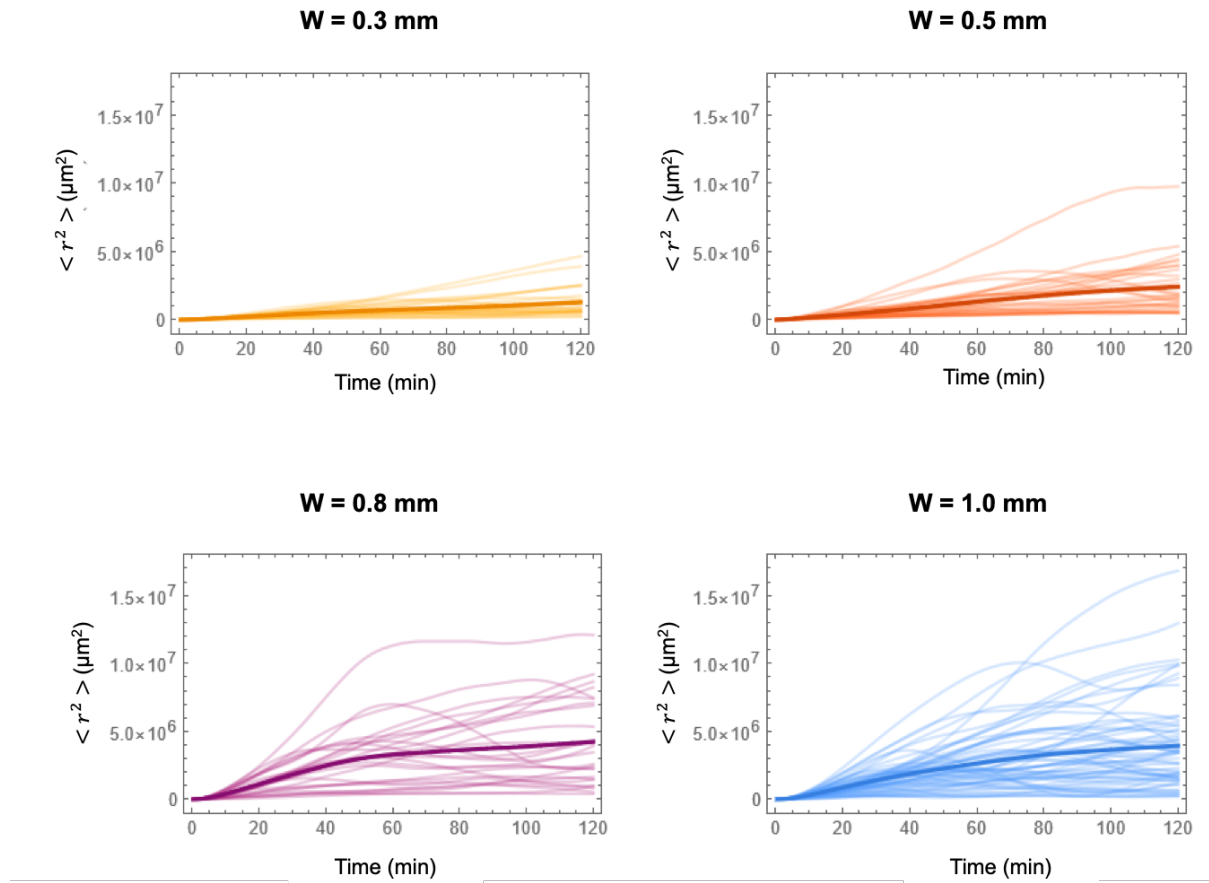


Figure S9 – Fiducial beads Mean Square Displacement. Each low opacity line corresponds to an average over time for one single bead. It is taken over all moving windows of 2h for a single full 3h trajectory. Darker lines correspond to averaging over all beads. Only this final average is plotted in Fig. 2E

Ballistic and Diffusive regimes

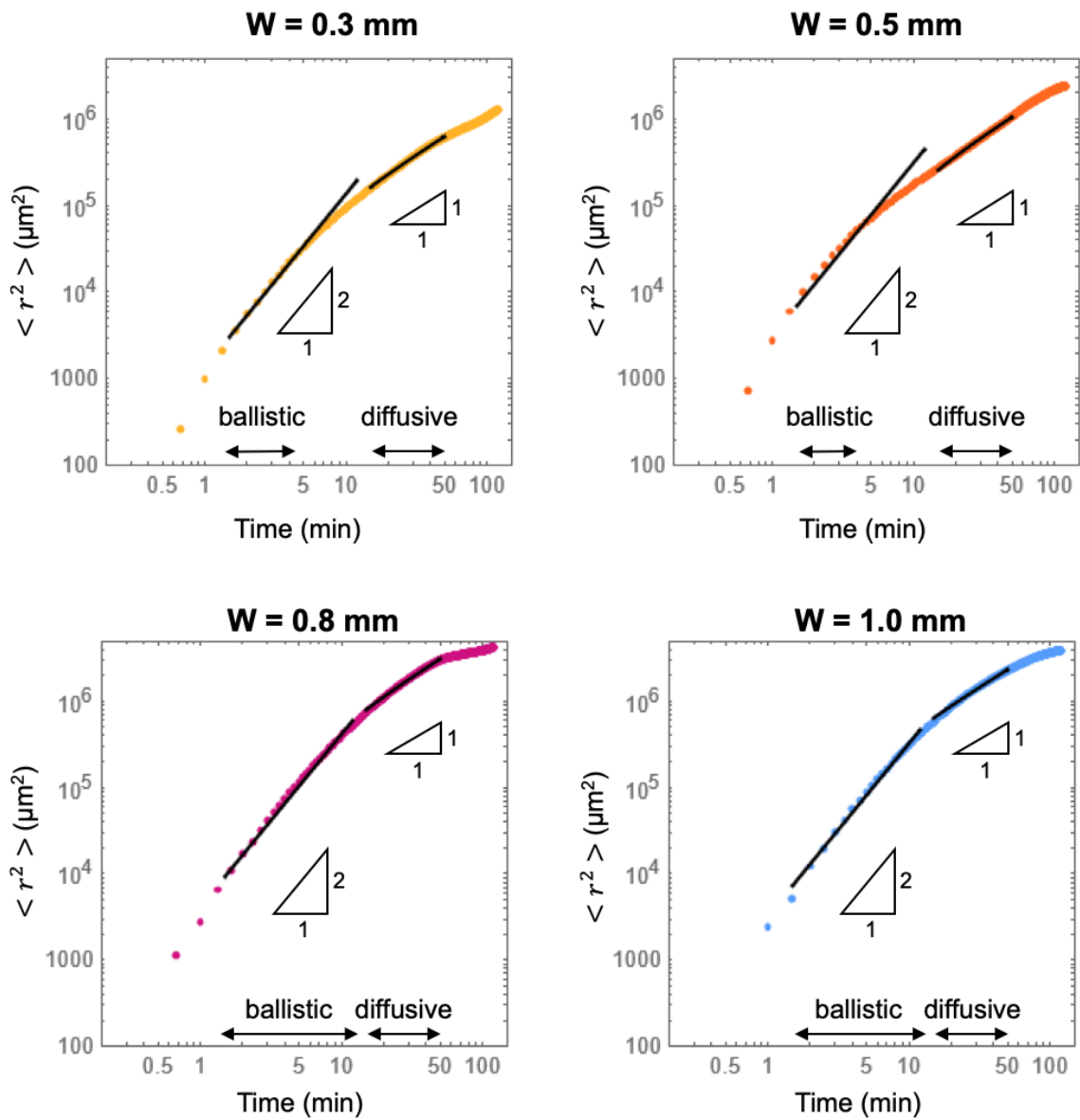


Figure S10 – Power law fits on beads Mean Square Displacement. A slope of 1 in this Log-Log plot corresponds to a diffusive transport while a slope of 2 to a ballistic one.

Reaction-Diffusion-Advection in channels of varying width

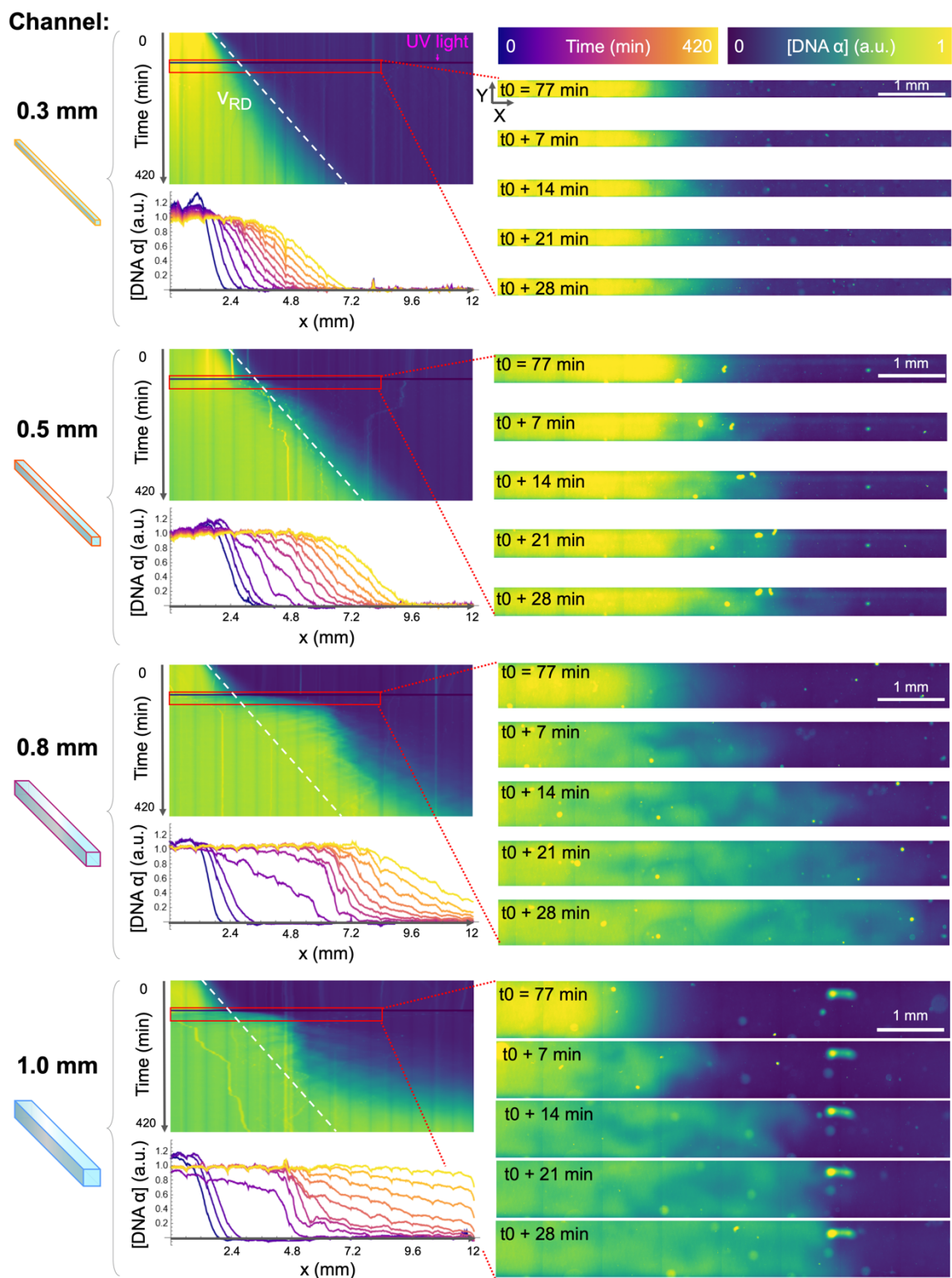


Figure S11– Geometry-dependent Reaction-Diffusion-Advection. Kymographs allow to compare the change in speed. Concentration profiles show the change in sharpness.

Active chaotic flows of kinesin-driven microtubules

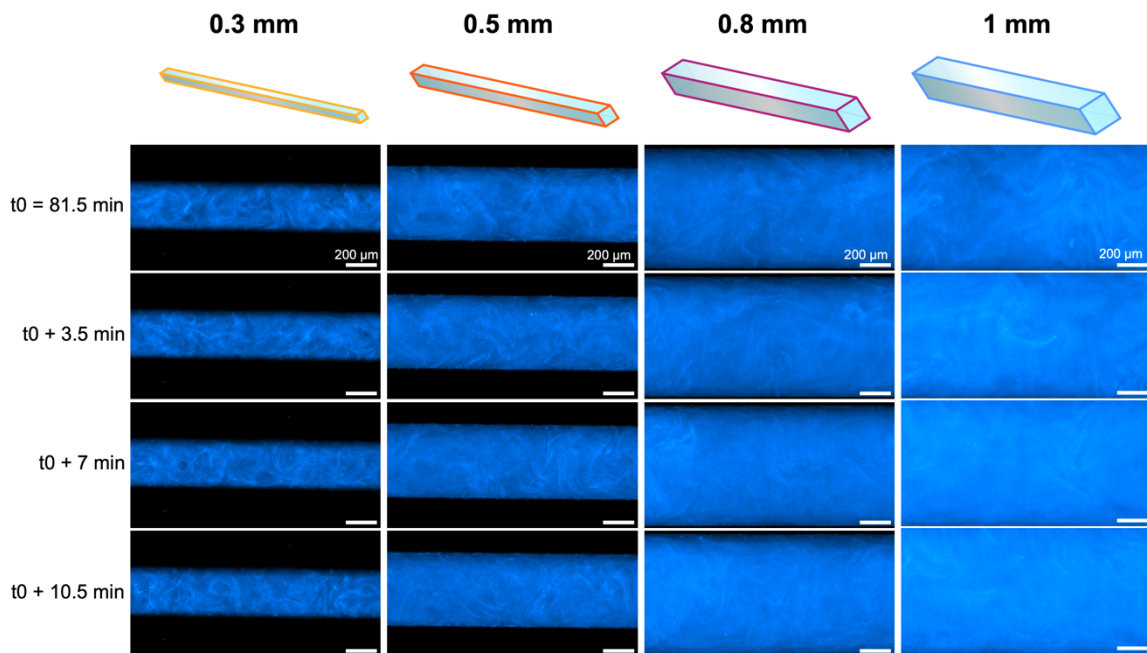


Figure S12 – Time-lapse of motor-driven microtubules for varying channel widths. Fluorescence is normalized by channel depth. Local configuration of microtubule bundles is very similar across channels. Microtubule bundles move in a chaotic manner.

Piecewise decomposition of front propagation over time

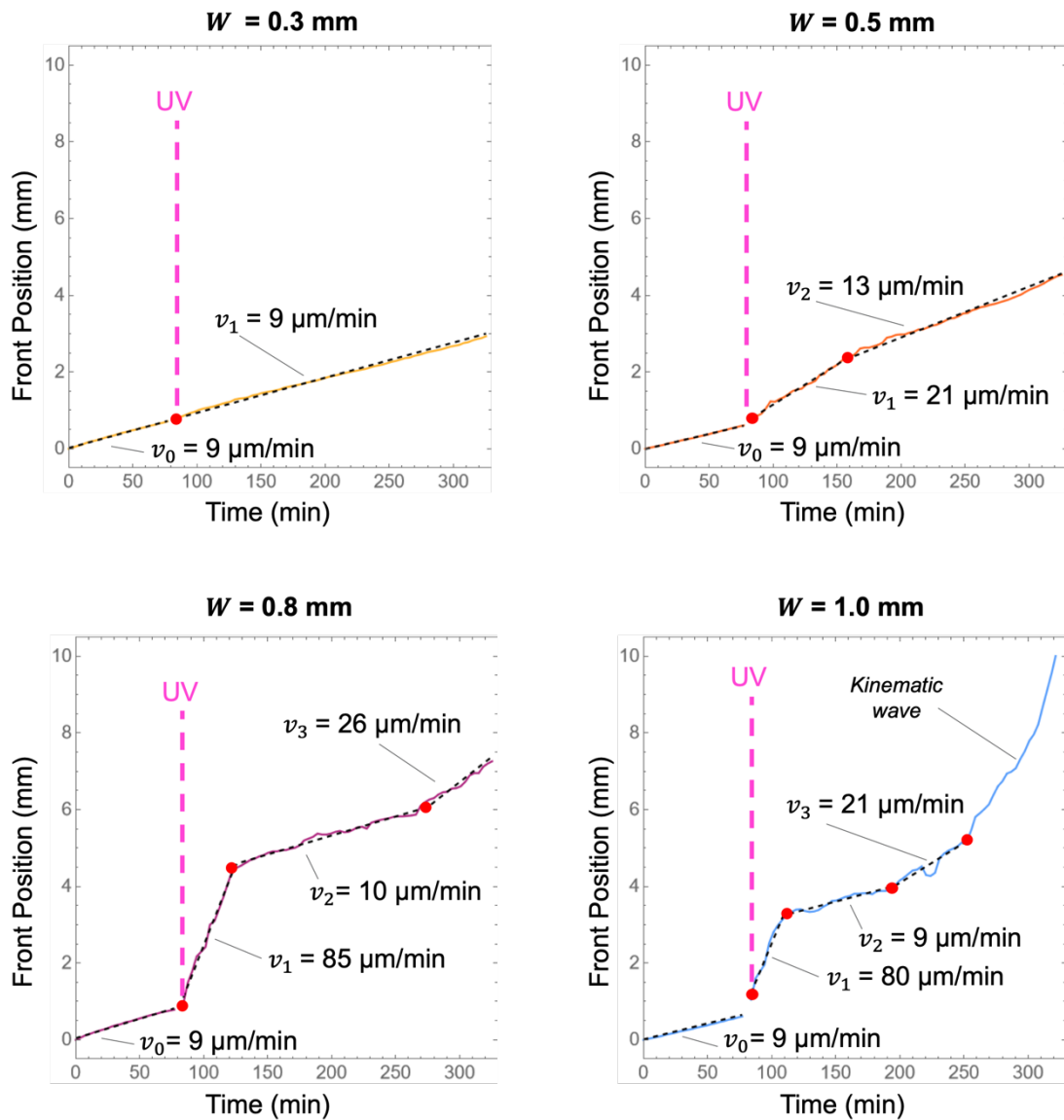
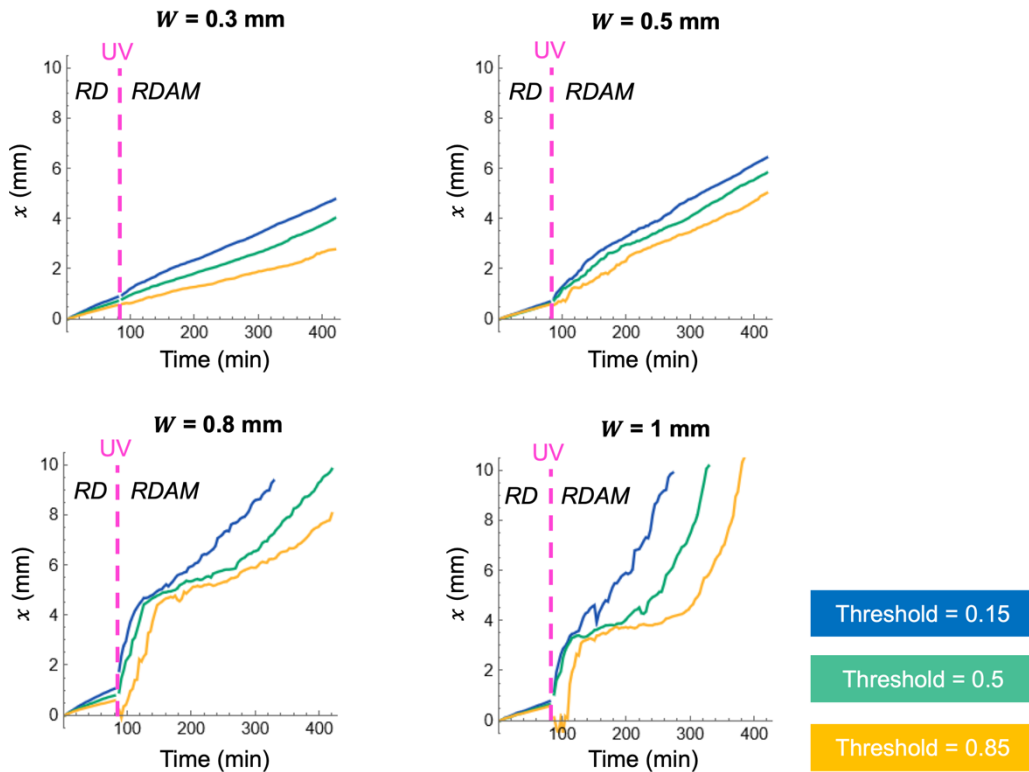


Figure S13 – Piecewise linear fits of front propagation in channels of different widths.

A

Front propagation depending on threshold choice



B

Definition of sharpness and speed

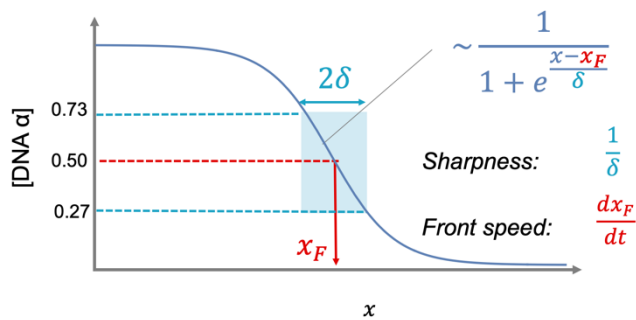


Figure S14 – Front speed and width depending on definition choices. A: Evolution of front position for different channel widths depending on concentration threshold. **B:** Sketch of the DNA front profile with definitions of the sharpness ($1/\delta$), the front position (x_f), and the speed. Taking 0.27 and 0.73 as thresholds allows to easily extract δ .

Evolution of the front speed and width over time

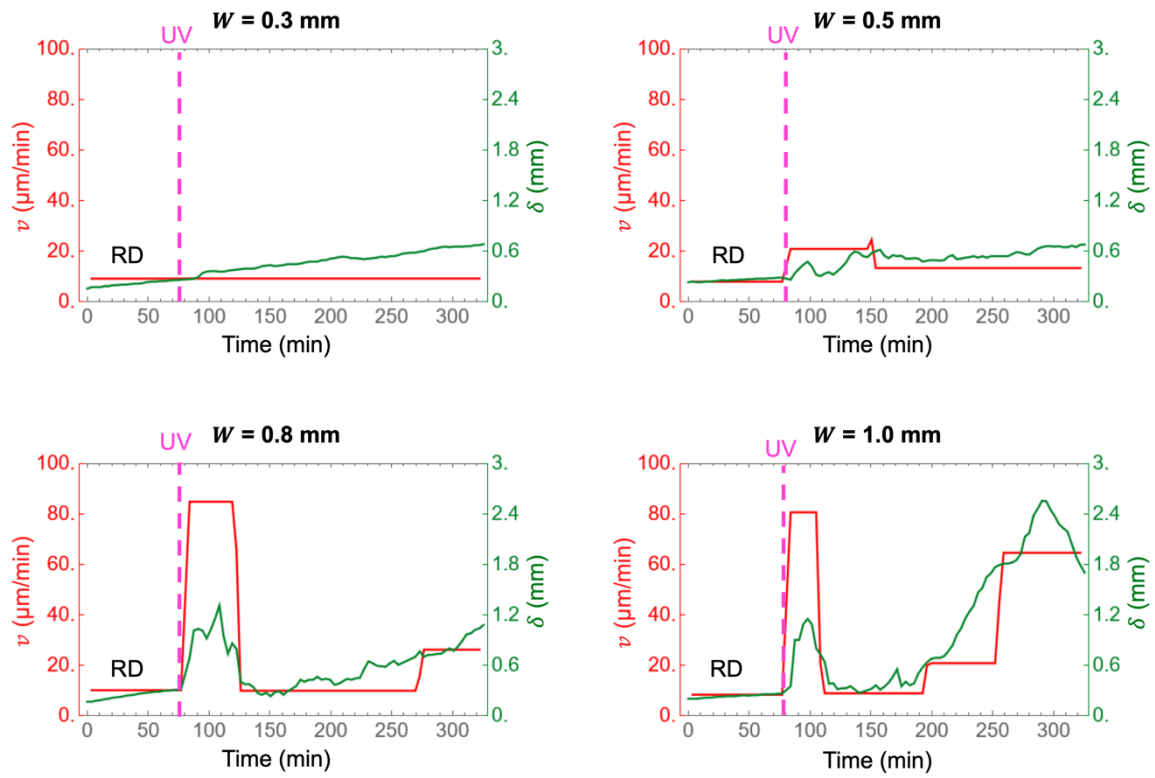


Figure S15 – Effect of channel geometry on the evolution of front speed and width.

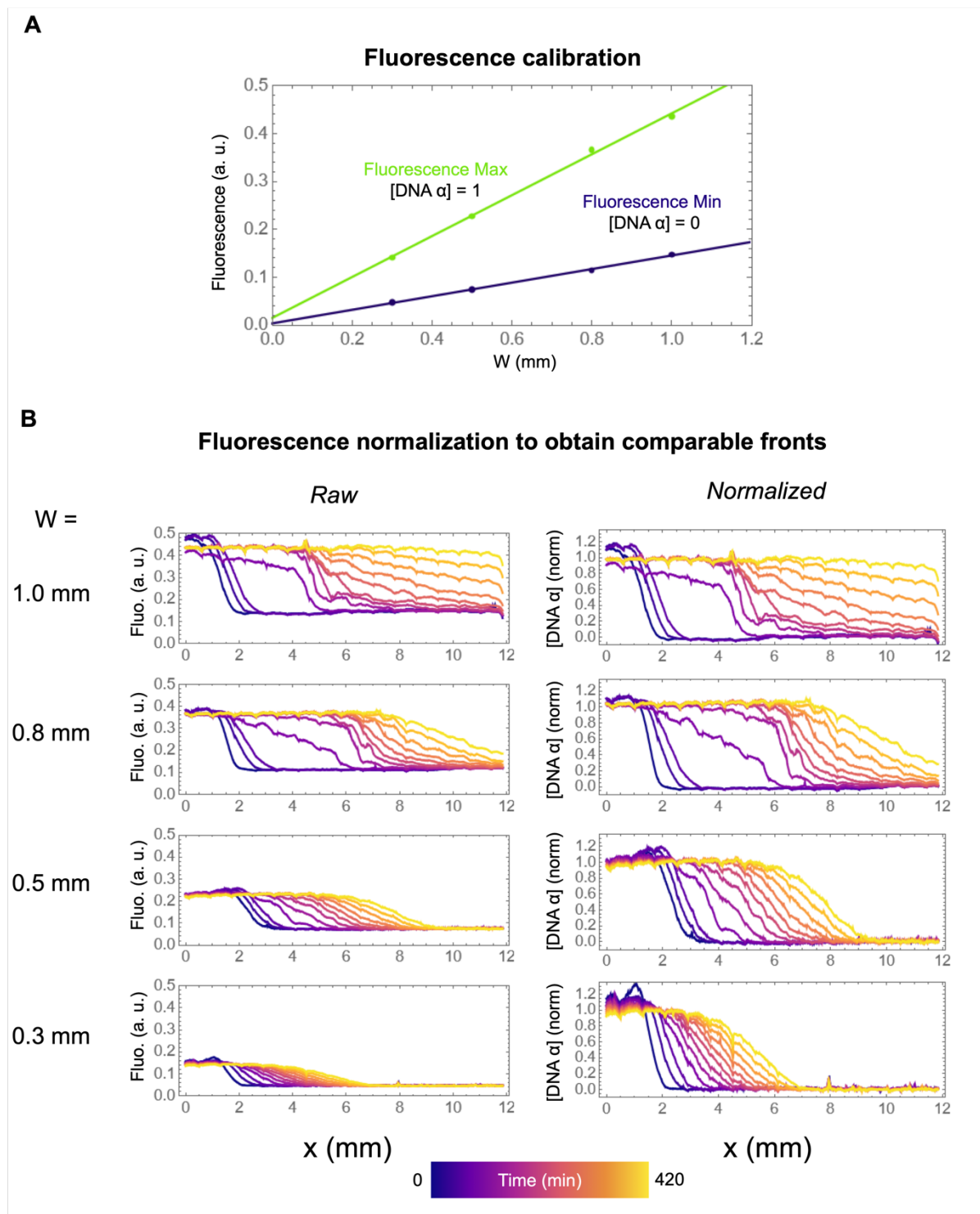


Figure S16 – Fluorescence normalization taking into accounts the varying channel heights. **A:** Calibration of the fluorescence in each channel using the high steady state and background fluorescence levels. **B:** Comparison of the raw and normalized fluorescence curves.

2. Supplementary Tables

Component	Concentration
PEM buffer (pH=6.9 KOH adjusted)	0.6 x
PEM buffer (pH=7.2 NaOH adjusted)	0.2 x
MgSO ₄	8 mM
Depletant (Pluronic)	1.5% (w/v)
NPE-Caged ATP	2 mM
Creatine Phosphate	5 µg/mL
Creatine Kinase	10 mM
DTT	3 mM
Glucose oxidase	150µg/mL
D-glucose	20 mM
Catalase	25 µg/mL
Trolox	1 mM
BSA	0.5 mg/mL
dATP	10 µM
dGTP	25 µM
dCTP	500 µM
dTTP	500 µM
SYBRGreenI	0.4 x
T _{αα}	100 nM
α	0 or 1 µM
Polymerase (BST Large Fragment)	0.5 % (v/v)
Nickase (Nt. BstNBI)	1.5 % (v/v)
Kinesin motors (BCCP kinesin)	75 nM
Streptavidin	75 nM
Microtubules	1 mg/mL

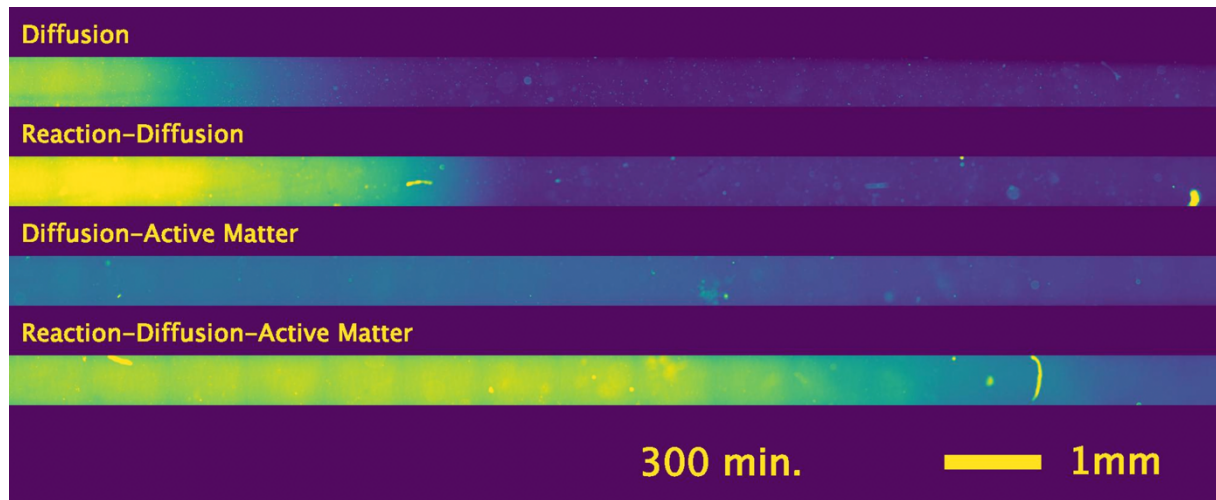
Table S1: Standard Active mix composition. This corresponds to Fig. 3-4. In Fig.1 α was injected at 10 µM for a better visualization and Polymerase or Kinesin were not added in some channels. In Fig. 2, T_{αα}, α, enzymes were replaced with Beads for tracking.

Name	Sequence (5'-3')	Modif. 5'	Modif. 3'
α	CGAGTCTGTT	∅	∅
T _{αα}	A*A*CAGACTCGAACAGACTCG	∅	Phosphate

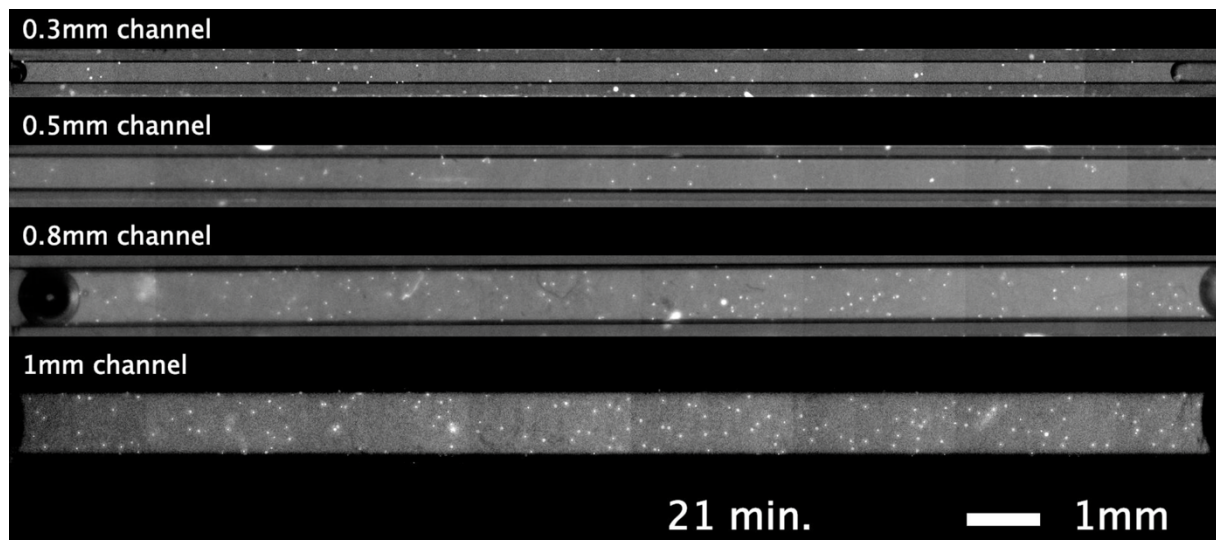
*phosphorothioate backbone modifications on the 5'

Table S2: Sequences of oligonucleotides

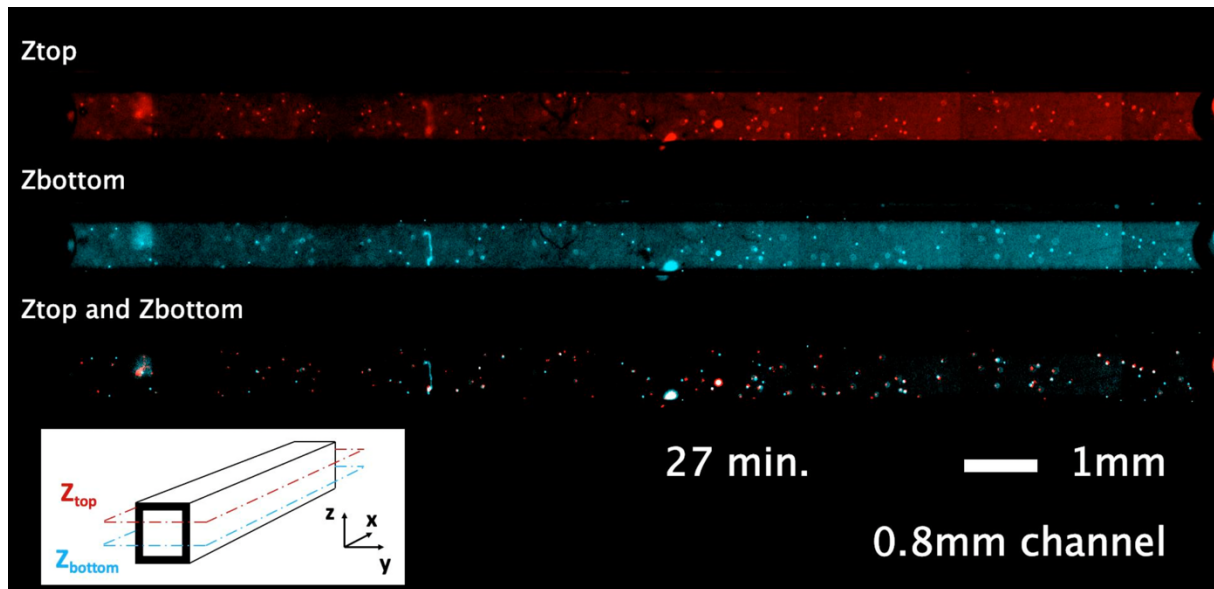
3. Legends of Supplementary Movies



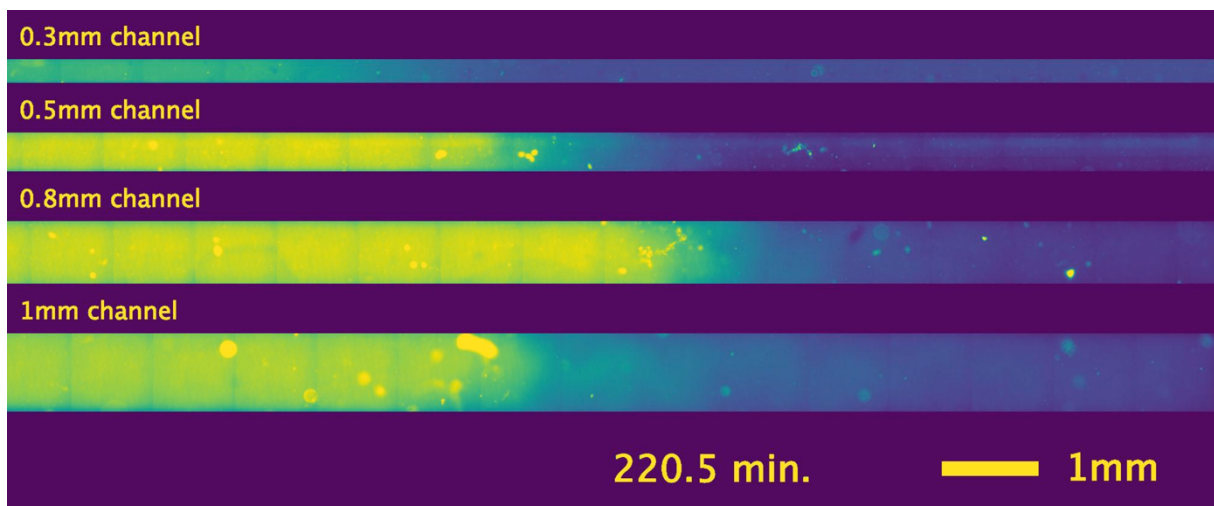
Movie S1 - Comparison of different Reaction-Diffusion-Advection configurations. Time-lapse images analyzed in Figure 1D,E. and Figures S3-6. Intensity corresponds to $[DNA \alpha]$ via fluorescence of Sybr Green I.



Movie S2 - Trajectories of fiduciary beads in channels of different widths. Time-lapse images analyzed in Figure 2. For $W=0.8$ mm and $W=1$ mm channels, images taken at different heights are summed to avoid losing focus.



Movie S3 - Trajectories of fiduciary beads in a 0.8 mm channel at two different heights. Beads at different heights go in opposite directions. Time-lapse images analyzed in Figure 2.



Movie S4 - Geometry-dependent Reaction-Diffusion-Advection. Time-lapse images analyzed in Figure 3-4. Intensity corresponds to $[DNA \alpha]$ via fluorescence of Sybr Green I. At $t_0 = 77 \text{ min}$, the channel is exposed to UV light which triggers advection.

Theoretical supplement: Linear stability analysis of aligned active fluids in three-dimensional channels

In this supplementary section, we describe the flows and instabilities of a three-dimensional channel filled with microtubule filaments and kinesin motors. The microtubules are initially aligned by flow while filling the channel with the gel and, in the absence of *active* motors, remain aligned. We model the microtubule gel as a three-dimensional nematic fluid oriented along \hat{x} and consider the effect of activity on this state [1-4]. This is somewhat distinct in detail (though, ultimately not in the end result) from [5,7] who assume that the orientational order decays with time. We believe that this distinction arises from the differing microscopic details in the experiments such as the bundle thickness and the density. Indeed, we and others [4, 8-10], showed in earlier works that changing the composition of the gel—such as the amount of ATP or motor concentration—dramatically changes its physical properties.

We characterise the ordered state by the nematic order parameter $\mathbf{Q} = \mathbf{nn} - (\mathbf{I}/3)$, where \mathbf{I} is the identity tensor and \mathbf{n} is the director which is a unit vector that points along the microtubules. The fluctuations about the nematic state is parametrised by the director as $\mathbf{n} \approx (1, \delta n_y, \delta n_z) \equiv (1, \delta \mathbf{n}_\perp)$, with the perfectly ordered state being $\mathbf{n}_0 = \hat{x}$.

The evolution of the fluctuations of the director field $\delta \mathbf{n}_\perp$ about its ordered state is described by the standard dynamical equation [11, 12]

$$\partial_t \delta \mathbf{n}_\perp = \frac{1-\lambda}{2} \partial_x \mathbf{v}_\perp - \frac{1+\lambda}{2} \nabla_\perp v_x + \Gamma K \nabla^2 \delta \mathbf{n}_\perp, \quad (1)$$

where \mathbf{v} is the velocity field of the microtubule gel and $K \nabla^2 \mathbf{n}_\perp = -\delta F / \delta \mathbf{n}_\perp$ with the free energy $F = (K/2) \int (\nabla \delta \mathbf{n}_\perp)^2$ in the single Frank constant approximation [11, 13]. The coupling of the velocity field to the director fluctuations has two parts [11, 12]: i. the director field is rotated by the vorticity field $(1/2)[\partial_x \mathbf{v}_\perp - \nabla_\perp v_x]$ and ii. the director field also experiences a torque in response to a strain-rate [11, 12] $(1/2)[\partial_x \mathbf{v}_\perp + \nabla_\perp v_x]$. The coefficient λ for this latter coupling is phenomenological (and not fixed by rotation invariance unlike the coupling to vorticity); if $|\lambda| < 1$, the system is flow-tumbling and if $|\lambda| > 1$ it is flow-aligning.

For slow flows, relevant for all microbiological materials, inertia is irrelevant and we balance viscous forces with other active and passive force densities due to the motor-microtubule gel to construct the linearised, constitutive equation for the velocity field:

$$\eta \nabla^2 \mathbf{v} = \nabla \Pi - \zeta (\nabla_\perp \cdot \delta \mathbf{n}_\perp \hat{x} + \partial_x \delta \mathbf{n}_\perp) + \zeta_2 \nabla^2 [(1/3) \nabla_\perp \cdot \delta \mathbf{n}_\perp \hat{x} - (2/3) \partial_x \delta \mathbf{n}_\perp] + \frac{1+\lambda}{2} \nabla_\perp \cdot \frac{\delta F}{\delta \mathbf{n}_\perp} \hat{x} - \frac{1-\lambda}{2} \partial_x \frac{\delta F}{\delta \mathbf{n}_\perp}, \quad (2)$$

where Π is the pressure that enforces the incompressibility constraint $\nabla \cdot \mathbf{v} = 0$. There are two active force densities in this equation. The first $\propto \zeta$ is the standard active dipolar force density, with $\zeta < 0$ being extensile (which corresponds to motor-microtubule gels) and $\zeta > 0$ being contractile, and the second $\propto \zeta_2$ is a higher order in gradients active force density. It is irrelevant in a bulk fluid where the dynamics is controlled by ζ , but *not in a confined geometry*. There are also other active force densities at this order in gradients, such as $\nabla^2 (\nabla_\perp \cdot \delta \mathbf{n}_\perp \hat{x} + \partial_x \delta \mathbf{n}_\perp)$. We choose to retain just this because i. while we do want to highlight the importance of retaining higher order in gradient active stresses for understanding the dynamics of confined active fluids, we don't aim at a quantitative calculation of the active flow in such a geometry and ii. it was shown [4] that this active force density qualitatively modifies the character of the active instability—changing its threshold and even eliminating it completely—and active flows in confined geometries. Note that both ζ and ζ_2 are likely to depend on the same parameters microscopically. Dimensionally, ζ_2 contains two extra powers of lengths which are likely to be proportional to a lengthscale associated with the microtubule filaments. The last two terms in [2] are passive force densities arising from director distortions and is required for relaxation to a steady state distribution $\propto e^{-F}$ in the absence activity [11, 12].

We now Fourier transform [1] and [2] in space and time, with ω being the frequency and $\mathbf{q} \equiv (q_x, q_y, q_z) \equiv (q_x, \mathbf{q}_\perp)$ being the wavevector of perturbation. Solving for the velocity field in terms of the director perturbation by eliminating the pressure using the transverse projector $\mathcal{P}_{ij} = \delta_{ij} - q_i q_j / q^2$, we obtain two coupled equations for δn_y and δn_z fluctuations. From this, we obtain the two eigenfrequencies which correspond to twist-bend and splay-bend modes (i.e., twist modes and splay modes with an admixture of twist):

$$\omega_{tb} = -i \left[\frac{\zeta}{2\eta} (1-\lambda) \frac{q_x^2}{q^2} - \frac{\zeta_2}{3\eta} (\lambda-1) q_x^2 + K\Gamma q^2 + \frac{K}{4\eta} (1-\lambda)^2 q_x^2 \right] \quad (3)$$

$$\omega_{sb} = -i \left[\frac{\zeta}{2\eta} \frac{q_x^2 - q_\perp^2}{q^2} \left(1 - \lambda \frac{q_x^2 - q_\perp^2}{q^2} \right) + \frac{\zeta_2}{6\eta} \frac{2q_x^2 + q_\perp^2}{q^2} \{ (\lambda-1) q_x^2 - (\lambda+1) q_\perp^2 \} + K\Gamma q^2 + \frac{K}{4q^2} \{ (\lambda-1) q_x^2 - (\lambda+1) q_\perp^2 \}^2 \right]. \quad (4)$$

The *negativity* of $-i\omega_{tb}$ and $-i\omega_{sb}$ ensures the stability of the orientationally ordered gel. That is, if *either* of the quantities in square brackets in (3) and (4) turn negative for some set of parameter values, the ordered state of the gel is unstable for that set of parameter values. Random fluctuations excite modes at all wavenumbers. An inspection of (4) reveals that to lowest order in wavenumber (i.e., for $q \rightarrow 0$), the eigenfrequency ω_{sb} is always destabilising for *some* wavevector directions (i.e., either $q_x \lesssim |q_\perp|$ or $q_x \gtrsim |q_\perp|$) irrespective of parameter values (2). However, for *extensile* $\zeta < 0$ active systems when $\lambda < 1$ (5, 6), ω_{tb} in (3) is *also* destabilising; in this case, the growth rate of the twist-bend mode dominates over the splay-bend one (5, 6) because it is unstable for all wavevectors with $q_x \neq 0$ while ω_{sb} interpolates to splay and is thus stabilised (14).

The value of λ need to be measured experimentally. There is no a priori reason to assign a specific value or even sign to λ for a particular system. It has, at times, been argued that λ must be small (i.e., $|\lambda| < 1$) in the ordered state. This is not necessarily justified. However, in equilibrium systems, in general, molecular nematics are flow-aligning (i.e. $|\lambda| > 1$) and larger objects are flow-tumbling (i.e., $|\lambda| < 1$). Further, rod-like objects usually have $\lambda < 0$ and disc-like objects have $\lambda > 0$ (15). Since microtubule bundles are rod-like and fairly large, and since multiple experiments (5, 6) and simulations in three-dimensional active fluids suggest that $\lambda < 1$ in motor-microtubule gels, we use this value in the discussion that follows.

In the experiment, the extensile active gel is in a channel with a square cross-section of size W . To examine the growth rate of the gel with this constraint, we replace q_\perp^2 by the smallest value it can assume: $q_\perp^2 = 2\pi^2/H^2$. Using this and noting that the channel is at least one order of magnitude longer than H , we obtain the wavelength of the fastest growing mode as

$$\lambda_f^2 = \frac{2W^2}{(W/l_a) - 1} \quad (5)$$

where we have defined the active lengthscale

$$l_a = \pi \sqrt{\frac{3K[4\Gamma\eta + (\lambda - 1)^2] + 4\zeta_2(\lambda - 1)}{3\zeta(\lambda - 1)}}. \quad (6)$$

Eq. (5) has the same form as in (5); the main difference is in l_a which now contains a second activity coefficient ζ_2 and fully accounts for passive stresses. From (5), we see that W must be larger than l_a for λ_f to be real i.e., the ordered state of the gel to be unstable. λ_f decreases with increasing W till $W = 2l_a$ and then increases with W , scaling as $\lambda_f \sim \sqrt{W}l_a$ for $W \gg l_a$. Note that ζ_2 is important for obtaining both the threshold beyond which the gel is unstable and the crossover scale that determines whether λ_f decreases with W or increases with W . In particular, ζ and ζ_2 are likely to depend similarly on motor density. Therefore, simply increasing the motor density may not lead to a decrease in l_a and, in a confined system, an active gel may not get destabilised for any motor concentration, as discussed in (4). Determining the values of ζ , ζ_2 etc. individually presents a difficult experimental challenge. Instead, l_a may, in principle, be determined from measurements of λ_f . Also recall that this calculation is only valid when the dominant instability is due to the twist-bend mode; if the dominant instability is via the splay-bend mode (i.e., is $\lambda > 1$), the wavelength of the fastest growing mode has a different, more complicated dependence on W .

Note further that for $W \gtrsim l_a$, λ_f is very large. Since the channel in our experiment has a finite length L , $\lambda_f < L$ for this mode to exist. For channels smaller than that, the ordered state of an active gel is unstable if and only if the mode $q_x^2 = \pi^2/L^2$ is unstable.

In our experiments, the flows get smoother as W is increased. This is clearly seen from the measurement of the temporal correlation of the direction of motion of Lagrangian tracers; the persistence time of the tracers goes from being around a minute to around 20min as W increases from 0.3 or 0.5mm to 0.8 or 1 mm. This immediately implies that the lengthscale of flow structures also significantly increase (by at least an order of magnitude) as W is increased. Since one may reasonably expect the size of vortices to scale as λ_f (though this is not necessary: the scale of structures formed at long times need not be given by the fastest growing mode of an instability that destroyed the original state; indeed, it is not in our system), this increase in the scale of flow structures should be an indication of an increasing λ_f with W which means $W \gg 2l_a$ in our experiments even for the smallest W .

While the qualitative increase in the size of flow structures with increasing channel dimensions is accounted for by the simple linear stability analysis displayed here, understanding detailed features of the flow require a numerical calculation of the active gel model in the channel geometry, which will be presented elsewhere. Here, we qualitatively discuss some features of the flow. Experimental measurements of the active flow demonstrate that the persistence time of the Lagrangian tracers and, therefore, the scale of vortices are roughly the same for channels with $W = 0.3\text{mm}$ and $W = 0.5\text{mm}$. The vortices are much larger for channels with $W = 0.8\text{mm}$ and $W = 1\text{mm}$, but again, roughly of the same size for these two values. This may be rationalised by assuming that the flow is organised in a vortex array

aligned along the x axis. Vortex arrays have been regularly obtained in simulations of active fluids [16, 18, 20]. The number of clockwise and anticlockwise rotating vortices must be the same to maintain zero net vorticity [16]. Further, number of vortices should be a function of the ratio L/W on general grounds and should increase with L/W . Ref. [16] obtains a linear relationship for a polar fluid in a two-dimensional rectangular channel with strong anchoring condition. Whatever the functional dependence of the vortex number on L/W , the vortex number only increases in the increment of 2. Therefore, when W doesn't change by a lot, the vortex number may not change and the flow structure may remain qualitatively unchanged. The fact that there seems to be two well-defined "cells" in 0.8mm and 1mm channels in which the velocity field is roughly along (or opposite to) \hat{x} separated by a region in which the velocity field is mostly in the directions perpendicular to \hat{x} supports the existence of two oppositely rotating vortices in these channels. At smaller confinements, there seems to be more vortices. A more quantitative and detailed theoretical and experimental account of the active flow will be presented elsewhere.

To summarise, the linear stability analysis of an ordered active fluid in a channel geometry demonstrates that for $W \gg \ell_a$, the wavelength of the fastest growing mode grows with W . Beyond the instability, we believe that the experimental observations point to the existence of an array of vortices along \hat{x} . Given that the wavelength of the fastest growing mode increases with W , it is natural for there to be fewer vortices at larger W ; in fact, we seem to observe just a pair of vortices in the 0.8 and 1mm channels. We believe that a channel with a cross section of 1mm would support a steady flowing state [17] were it not closed at the end. Since the vortex number cannot increase continuously but has to increase by 2, it is also natural that channels with similar W have the same number of vortices. However, it is important to note that the stability analysis fails to predict both the structure of the flow and the scaling of vortex size with W . The vortex size increases 10-fold upon a 3-fold increase of W , signifying it scales as W^2 , in contrast to the stability analysis which would predict a \sqrt{W} scaling.

-
- [1] M. C. Marchetti et al., Rev. Mod. Phys **85**, 1143 (2013)
 - [2] R. A. Simha, S. Ramaswamy, Phys. Rev. Lett. **89**, 058101 (2002)
 - [3] R. Voituriez, J.-F. Joanny, J. Prost, Europhys. Lett. **70**, 404 (2005)
 - [4] A. Maitra et al., Proc. Natl. Acad. Sci **115**, 6934 (2018)
 - [5] P. Chandrakar et al., Phys. Rev. Lett. **125**, 257801 (2020)
 - [6] M. Varghese et al., Phys. Rev. Lett. **125**, 268003 (2020)
 - [7] L. M. Lemma et al., PNAS Nexus **2**, 5 (2023)
 - [8] G. Sarfati et al. Soft Matter **18**, 3793 (2022)
 - [9] B. Najma et al., Nat. Commun. **13**, 6465 (2022)
 - [10] D. A. Gagnon et al., Phys. Rev. Lett. **125**, 178003 (2020)
 - [11] P. G. de Gennes, J. Prost, The Physics of Liquid Crystals, Clarendon Press (1995)
 - [12] H. Stark, T. C. Lubensky, Phys. Rev. E **67**, 061709 (2003)
 - [13] P. M. Chaikin, T. C. Lubensky, Principles of Condensed Matter Physics, Cambridge University Press (2000)
 - [14] R. Chatterjee et al., Phys. Rev. X **11**, 031063 (2021)
 - [15] S. A. Edwards, J. M. Yeomans, Europhys. Lett. **85**, 18008 (2009)
 - [16] P. Gulati, S. Shankar, M. C. Marchetti, Front. Phys. **10**, 948415 (2022)
 - [17] K.-T. Wu et al., Science **355**, 1284 (2017)
 - [18] A. Doostmohammadi et al., Nat. Commun. **8**, 15326 (2017)
 - [19] A. Doostmohammadi et al., Nat. Commun. **7**, 10557 (2016)
 - [20] S. Chandragiri et al., Phys. Rev. Lett., **125**, 148002 (2020)